Department of AERONAUTICS and ASTRONAUTICS
STANFORD UNIVERSITY

JACKIE O. BUNTING
R. S. DEVOTO

SHOCK TUBE STUDY OF THE THERMAL CONDUCTIVITY OF ARGON

Submitted by D. Bershader

JULY
1967

Supported by the
National Aeronautics and Space Administration
Grant NGR-05-020-091

SUDAAR
NO. 313*

*Also issued as SU-IPR Report No. 176 of the Institute for Plasma Research, Stanford University

SHOCK TUBE STUDY OF THE THERMAL CONDUCTIVITY OF ARGON

by

Jackie O. Bunting
R. S. Devoto

July 1967

SU-IPR-~~Report~~ ~~No.~~ 176*

*This report was also issued as SUDAAR ~~No.~~ 313 of the Department of Aeronautics and Astronautics

Institute for Plasma Research
Stanford University Stanford, California

ABSTRACT

The end-wall thermal boundary layer behind a reflected shock has been analyzed to determine the thermal conductivity of argon over the temperature range from 3150 to 9225°K. Pressures behind the reflected shock, assumed constant through the thermal layer, were chosen sufficiently high to suppress non-equilibrium and side-wall effects. Temperature profiles, computed from interferometric measurements of density, were compared with a numerical solution of the full non-linear thermal boundary layer equations assuming a temperature dependence for thermal conductivity of the form $K \alpha T^{\nu}$. Typically, 10 to 12 points were obtained in a thermal layer which was approximately 1.5 mm thick, with the nearest points approaching 0.2 mm from the wall. Refraction effects and related optical distortion precluded measuring closer to the surface. Values for the exponent ν in the power law were obtained by minimizing the root-mean-square deviation between the theoretical and experimental profiles. From 18 temperature profiles the average value obtained for ν was 0.668 ± .02. This value was compared with existing theoretical predictions and with other measurements. The results offer encouragement for similar studies at even higher temperatures where free electrons will affect the thermal transport.

ACKNOWLEDGMENTS

We would like to express our appreciation to Professor Daniel Bershader for his helpful advice and criticism during the various stages of this research program. We also gratefully acknowledge the assistance of the following persons: Dr. D. Baganoff for helpful criticisms, Mr. Tony Mulac for assistance in conducting the experiments, and Miss Andrea Dinsmore for typing the manuscript. This research was supported by the National Aeronautics and Space Administration under Grant NGR-05-020-091.

TABLE OF CONTENTS

LIST OF TABLES

LIST OF ILLUSTRATIONS

NOMENCLATURE

a & $b_{1,2,3}$	power series expansion coefficients
c_p	specific heat at constant pressure
D, D_y	test section depth; distortion
d	total deviation of refracted ray
$f(\eta), \bar{f}(\eta)$	non-dimensional density
h	enthalpy per unit mass; focal plane location
K	Gladstone-Dale constant
M	Mach number
MZI	Mach-Zehnder interferometer
N	usable number of fringes
n	index of refraction; fringe number
n_g	index of refraction of exit window
p	gas pressure
$\dot{q}_w$	wall heat transfer rate
S	fringe shift
T	temperature
t	time; thickness of exit window
V_I	incident shock velocity
V_R	reflected shock velocity
v	gas velocity normal to end wall
W	deviation of refracted light ray
y	distance from end wall

α,β	parameters in refractive error analysis; angle for end wall alignment procedure
δ	boundary layer thickness
ϵ	angle in refractive error analysis
η	similarity transformation
θ	normalized temperature
K	atomic thermal conductivity
λ	wavelength of light
ν	power law exponent for thermal conductivity
ρ	gas density
σ	standard deviation
τ	ionization relaxization time

SUBSCRIPTS

1	initial shock tube conditions
2	conditions behind incident shock
5	conditions behind reflected shock
w	conditions at end wall surface
B	conditions in thermal boundary layer
E	light ray entrance station
OPT	optical path
RMS,M	root-mean-square and mean deviation
R,BL,BS	fringe shift error notations, R - refractive error, BL - boundary layer error, BS - beam splitter error

1. INTRODUCTION

Fundamental to the understanding of most phenomena involving the flow of gases is a knowledge of the transport coefficients. These coefficients relate the flux of mass, momentum, and energy in a gas to gradients of some physical property through the gas. At the low gas temperatures (1000°C or lower), it is possible to measure with direct equilibrium type experiments most of the coefficients with accuracies of ± 0.1% or even better.[1] However, at much higher temperatures it is not possible to contain a gas for long periods of time, and it becomes much more difficult to measure transport coefficients. For this reason it has been necessary to rely almost exclusively on theoretical predictions of the coefficients especially in dissociating and ionized gases.[2] Although there have been some measurements of electrical and thermal conductivities in partially ionized argon[3] the poor precision of these measurements does not enable one to choose between different theoretical predictions of these properties. It is of obvious importance to seek new and possibly more accurate experimental methods for measuring transport coefficients in high temperature gases.

This report describes a quantitative optical technique for measuring the thermal conductivity of hot gases which can be generated in the end wall region of a shock tube. The technique utilizes the Mach-Zehnder interferometer (MZI) to analyze the flow field and the thermal boundary layer at the end wall after reflection of the incident shock wave. The process of reflecting a shock wave by a solid wall creates a slug of hot quiescent gas in thermal contact with a cold wall. At the interface

between the wall and the hot gas a thermal boundary layer develops and grows with time. This hot gas is well suited for studying thermal transport because it is essentially at rest and the effects of viscosity and mass diffusion are very small and generally negligible.

In this experiment the MZI is used to obtain density and temperature profiles through the thermal boundary layer in a quantitative manner. These profiles are then compared with theoretical predictions obtained from a numerical solution for the complete thermal boundary layer equations, assuming a relationship between thermal conductivity and temperature of the form $K \alpha T^{\nu}$.

The concept of using the quiescent body of hot gas behind the reflected shock wave to deduce thermal conductivity has been recognized for some time. Several investigators have performed experiments at the end wall surface as a means of deducing thermal conductivity. Smiley[4] was the first to use this region in his measurements of the total heat flux to the end wall surface and from these experiments he deduced values for the thermal conductivity of argon over the temperature range from 1000 to 3000°K. Hansen, Early, Alzofon and Witteborn[5], and Peng and Ahyte[6], made similar measurements in dissociated air. However, their analysis of the experiments was incorrect since they neglected the convection of gas toward the end wall induced by the cooling of the gas by heat transfer to the solid. Thomson[7] pointed out this error and gave the correct formulation of the equations. Ahyte and Peng[8] also corrected their analysis in a later publication. Collins and Menard[9] and Collins, Greif, and Bryson[10] measured thermal conductivities of several noble gases for temperatures up to 6700°K with this same heat transfer technique.

Camac and Fienburg[11] were able to deduce the thermal conductivity of atomic argon at temperatures up to 75000°K by measuring the heat flux at very early times after shock reflection where the gas ionization has not taken place. They also compared theoretical and measured heat transfer at later times when the ionization process was complete.

A completely different technique for deducing thermal conductivity was reported by Sturtevant and Slachmuylders.[12] They were able to measure the effect of heat transfer to the end wall on the reflected shock trajectory. That is, as the gas adjacent to the wall is cooled by heat transfer, the density near the wall increases. In order to supply the necessary mass a displacement velocity toward the wall is induced in the hot gas. This motion perturbs the trajectory of the reflected shock and the magnitude of this perturbation is related to a Reynolds number based on time after shock reflection. The thermal conductivity can then be deduced from the Reynolds number correlation between theory and experiment.

The alternative approach proposed in this study has been used for experiments in air by Smeets[13], where he obtained a profile of refractive index in the outer portion of the thermal layer with a differential interferometer.[14] His results extend over a temperature range from 1140 to 6075°K where the effects of oxygen and nitrogen dissociation appear at about 2000 and 4000°K respectively. His experimental results were compared with a theoretical profile obtained from a solution of a linearized form of the governing equations which is accurate only in the outer region of the thermal layer.

The optical interference technique used here, although similar to

that of Smeets, is different in two important respects: First, a numerical solution of the full end wall boundary layer equations is used to compare theory with experiment and second, the MZI allows more freedom in fringe orientation than does the differential interferometer. This feature of the MZI can be used to good advantage in resolving the density and temperature profiles in the thermal layer. The experiments presented here use argon as a test gas and the temperature ranges from 3150 to 9225°K, where the degree of ionization is still negligible. Experimental temperature profiles are compared with theoretical predictions and a value for ν is obtained by minimizing the root-mean-square deviation between the two.

This discussion is divided into seven chapters. The second chapter describes the shock tube and associated optical equipment. Chapter 3 gives a brief outline of the end wall boundary layer theory followed in Chapter 4 by a discussion of the experimental parameters important in designing this type of experiment. Chapter 5 presents the results of the initial calibration experiments and describes the final method used to resolve the boundary layer profiles. In Chapter 6 the refractive error analysis derived in Appendix B is applied to the specific case of the end wall boundary layer. The final chapter contains the conclusions based on the results presented in Chapter 5. In Appendix A the method used for aligning the end wall with the MZI test beam is described while Appendix C contains a discussion of the side wall boundary layer effects.

2. EXPERIMENTAL APPARATUS

2.1 Shock Tube

The general features of the operation of a shock tube have been discussed extensively in the literature[15-17] and will not be repeated here. However, some aspects of the instrumentation and shock tube design which are important for these studies will be discussed. The basic facility, shown schematically in Fig. 1, has been described in some detail by Wong.[18] The driven section, made from extruded aluminum, is 6.7 meters long with a 5 cm by 5 cm square interior cross section. The square cross section is particularly convenient for interferometric studies because it provides an essentially two dimensional flow field which simplifies the analysis of interferograms. The driver section of the tube is made of stainless steel with a 7.6 cm internal diameter and 3.8 cm walls. A short transition section is located just downstream of the diaphragm station to provide a smooth transition from the circular driver section into the square driven section. The driver chamber is designed for use with either combustion heated drive or pure pressure drive. For these experiments the pure pressure drive feature was used with helium as the driver gas.

Prior to a run each chamber of the tube was evacuated with separate mechanical vacuum pumps. The pressure in the driven chamber, before filling with argon, was lower than 2×10^{-3} Torr as measured by a Pirani vacuum gauge (CEC). The initial loading pressure of the test gas was monitored with a Wallace and Tiernan vacuum gauge which was calibrated periodically with a standard McLeod gauge. The leak rate of the driven tube and its associated hardware was 0.2 microns per minute; thus, for a

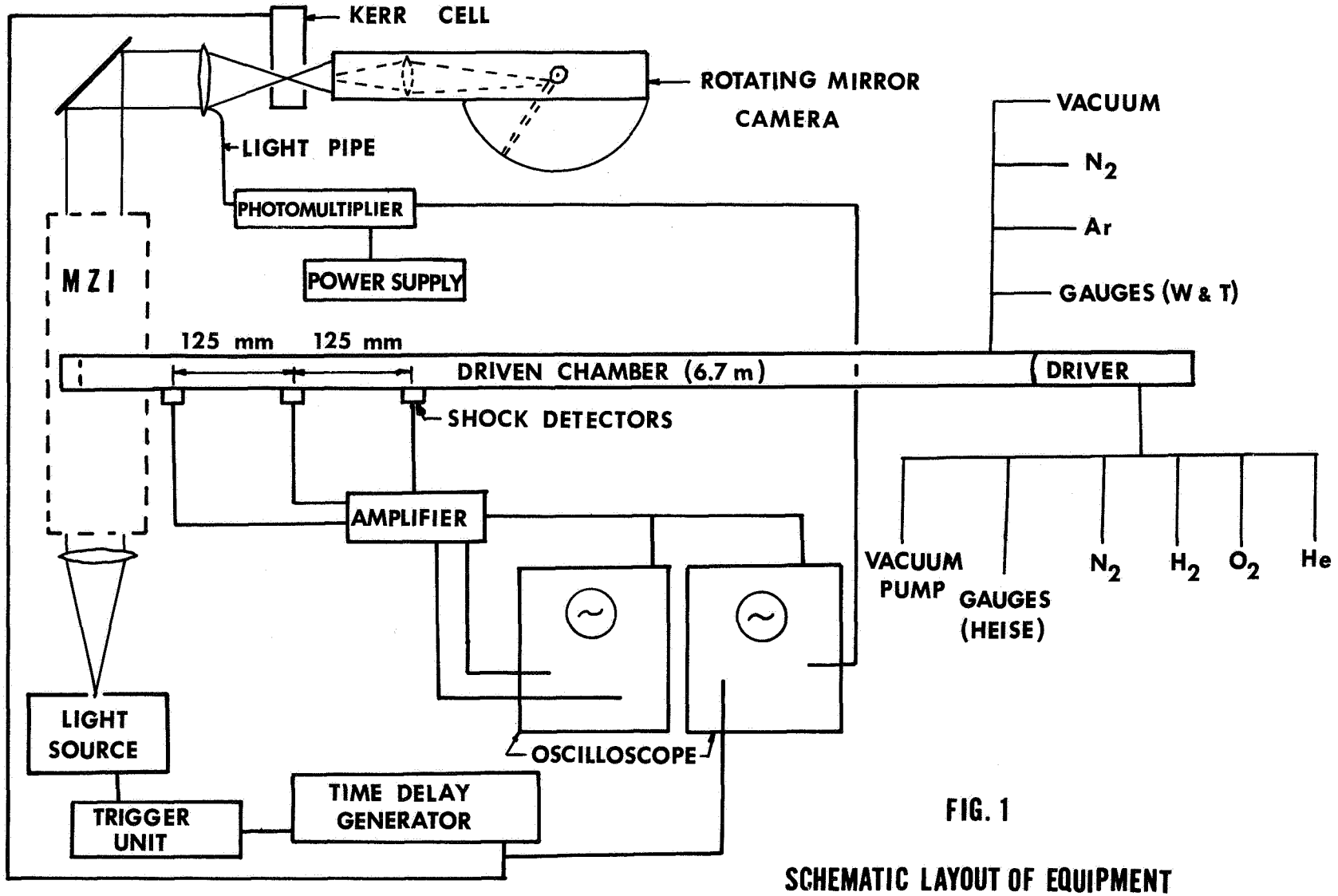

FIG. 1

SCHEMATIC LAYOUT OF EQUIPMENT

typical elapsed time of five minutes between filling the driven chamber and firing the tube the impurity level is 1.0 microns or 0.01% for 10 Torr initial pressure.

Three stations 125 mm apart are provided for measuring the initial shock velocity with the last station located 134 mm from the end wall surface. When thin-film gauges were used for shock detection, the signals were amplified before display on the oscilloscope. The initial calibration experiments were conducted with barium titanate pressure transducers as shock detectors. These proved unsatisfactory for the low shock Mach numbers desired ($M < 8$) because pressure signals traveling in the walls of the tube reach the gauge before the shock wave. Some of the later calibration experiments and all of the boundary layer experiments were conducted using thin film heat transfer gauges as shock detectors. Transit times between the gauges were measured to within $\pm$ 1 μsec on an oscilloscope that was calibrated against a Time Mark Generator accurate to 0.001%. The distance between two gauges is known to within $\pm$ 1 mm which corresponds to the width of a gauge filament. These two contributions give rise to an uncertainty in initial shock Mach number of slightly less than 2%. This uncertainty in Mach number results in a 2 to 3% uncertainty in the predicted temperature behind the reflected shock. The three pickup stations are used to give independent checks on the shock velocity as well as shock attenuation. No attenuation was detectable for these experiments.

2.2 MZI* and Associated Equipment

The construction and operation of the Mach-Zehnder interferometer is conventional and will not be discussed in detail as there are many excellent descriptions of the problems of design, construction, and adjustment of this type of instrument.[19,20] Figure 2 shows a photograph of the test equipment and the MZI which is mounted with its plane of centers perpendicular to the axis of the shock tube. The upper beam passes through two windows mounted at the shock tube test section and the lower beam passes through a matched pair of windows in the compensating beam. Both the test section windows and the compensating windows are made of optically flat $(\lambda/4)$ schlieren quality quartz with faces parallel to within 0.0005". The lens (focal length 71 cm) shown mounted next to the beam splitter on the interferometer framework is used to collimate the light from the light source.

The light source used for this study is an exploding tungsten wire which is located at the focal point of the collimating lens. Figure 3 shows a circuit diagram of the essential features of its design. It consists of a 0.005" diameter tungsten wire supplied by a 7.5 microfarad fast discharge capacitor charged to 20 kv. A 50 volt pulse from the time delay generator (shown in Fig. 1) initiates a trigger unit which produces a 15 kv pulse to break down a sealed spark gap switch. This type of light source has been used by several other investigators[18,21,22] for interferometric studies. The rise time, for the particular circuit used here, has been established from photomultiplier signals as 2 μsec while the radiation persists for longer than 200 μ sec.

*This interferometer was on loan through the courtesy of Lockheed Missiles and Space Company Research Laboratory, Palo Alto, California.

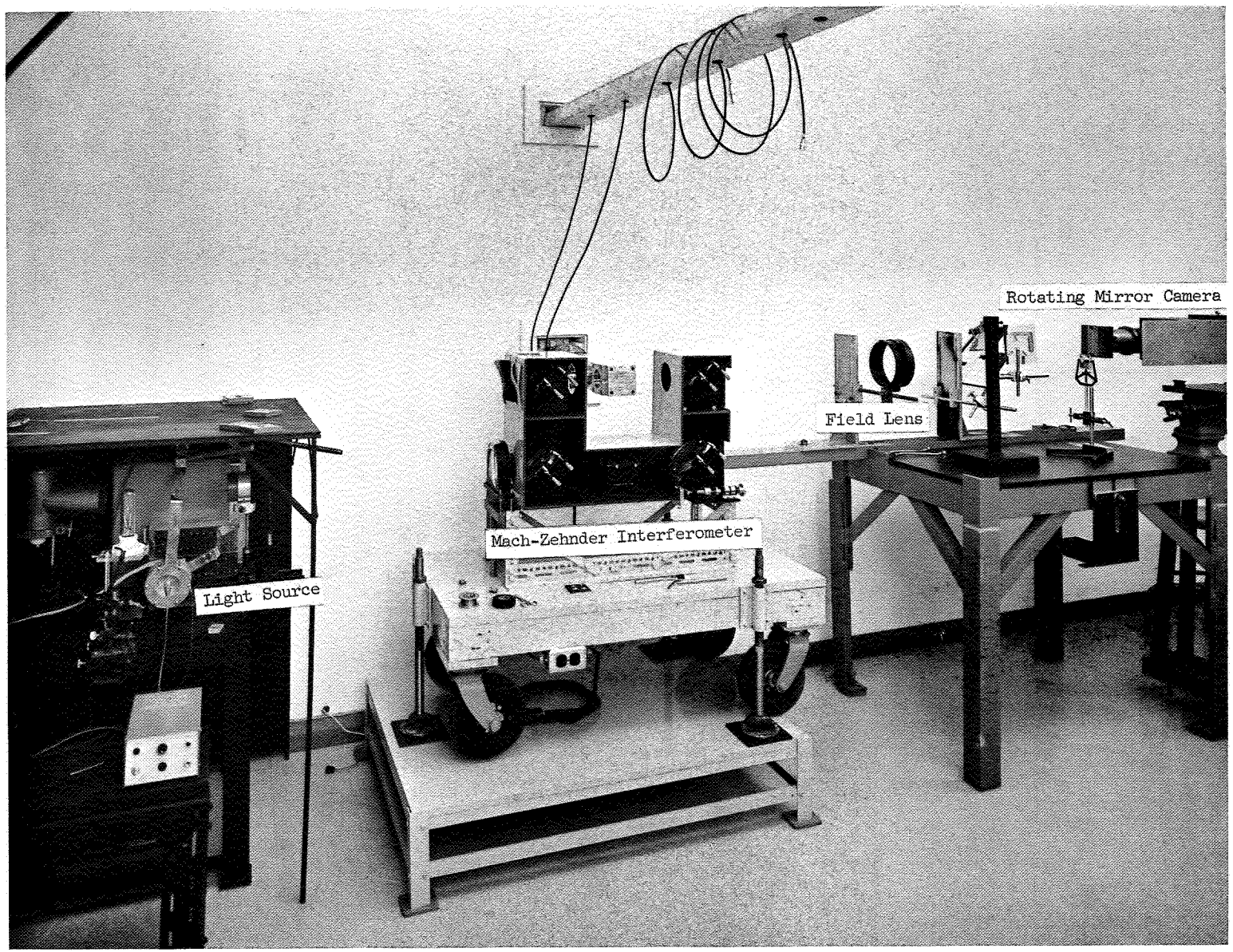

Fig. 2. Photograph of Experimental Equipment

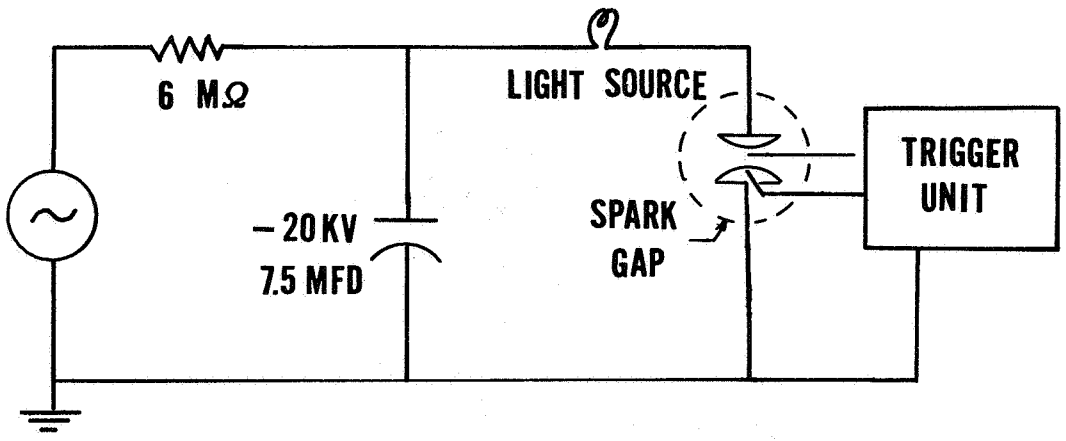

Fig. 3. Schematic of Exploding Wire Circuit

As can be seen by the light intensity fluctuations in Fig. 6 this arrangement has a characteristic ringing frequency due to the natural self ringing of the capacitor and associated circuit. For this set up this frequency was 145 kc/sec as compared with 300 kc/sec for the natural self ringing frequency of the capacitor. That the observed ringing frequency is lower than that of the supply capacitor is to be expected because of the increased inductance produced by the copper strap leads necessary to form a complete circuit.

The large burst of light from the exploding wire is localized by means of a slit (or circular aperture in some experiments), which is mounted approximately 2 mm from the tungsten wire. The significance of the use of a slit instead of the circular aperture is explained in the discussion of the experiments. In effect the slit (or aperture) defines the location of the light source and it must be located at the focal point of the collimating lens. Two different types of interferograms were taken during the course of this investigation. The initial calibration experiments were performed using time-resolved interferograms

recorded with a rotating mirror camera (shown in the photograph of Fig. 2). Later experiments to resolve the boundary layer profile used snap-shot records. The snap-shots were taken using the exploding wire in conjunction with a Kerr-cell electro-optical shutter. Exposure times of 1 and 2 μ secs were used for the latter records.

The technique of time-resolved interferometry, using a rotating mirror camera, have been used often in the past for studying the time history of transient phenomena.[21,23,24] The idea is to sweep a very narrow image of the test section slit together with the fringes, focused in the test section, across a stationary strip of film by rotating a mirror at very high speeds. Resolution times for this technique are determined by the width of the image and the writing speed at the film plane. With a typical writing speed of 3 mm/μsec and a slit width of 0.5 mm one obtains a resolution of 0.16 μ sec. This particular camera has a hexagonal stainless steel mirror with each face polished flat to 1/2 wavelength. The mirror is mounted on a dynamically balanced shaft and driven by an air turbine motor to speeds of 700 rps.

A single 3" diameter f/2.5 lens was used to focus the fringes at the desired location in the test section. This is not an optimum situation since one would prefer to use a separate camera lens in conjunction with the field lens in order to make the magnification of the optical system less sensitive to the distance between the focal plane of the test section and the field lens. However, when a single camera lens is used it is difficult to magnify the test section image and a third lens must be used to obtain reasonable magnifications (~ 2). Light source limitations precluded the use of two additional lenses.

The one feature not shown in the photograph (see Fig. 2) but used in all experiments is the interference filter mount. The physical location of the filter was not critical but it was convenient to locate it between the field lens and the film plane. The time-resolved calibration experiments were performed with narrow band pass (100Å) interference filters. These filters have a transmission of approximately 25% of the incident light intensity. This transmission, although satisfactory for the time-resolved experiments, was not adequate for the snap-shot records because of the additional light attenuation at the Kerr-cell. In order to increase the transmission it was necessary to use a combination of two interference filters (each having an 80% transmission) where one transmits only low wavelengths and the other only high wavelengths. By choosing two filters where the transmissions overlap it is possible to construct a high transmission (60%) filter with subsequent increase in transmitted band width (800Å).

The effective wavelength to be used for a particular combination was determined in the following manner: First an interferogram is taken with a known monochromatic light source (Hg arc, 5460Å) and the fringe spacing is carefully measured. From this the angle of apparent intersection between the two interfering beams can be computed from the relation

$$W = \frac{\lambda}{\varphi}, \tag{2.1}$$

where W is the fringe spacing and λ the known wavelength of the light source. Next without disturbing the interferometer or optical system an interferogram is taken with the exploding wire substituted for the monochromatic light and a filter inserted in the light path. The

new fringe spacing is then measured and since φ is constant an effective value of λ can be computed from Eq. (2.1). By this method a value of 4690 ± 50Å was obtained for the combination used here and this value is well within the expected value given by the manufacturers transmission curves for the separate elements. The usable number of fringes which one can expect with a broad band-pass filter of this type can be obtained from an expression given by Tanner.[25] For an effective wavelength given by $\lambda = \lambda_0 \pm 1/2(\lambda_1)$ the usable number of fringes is given by

$$N = C \frac{\lambda_0}{\lambda_1} . \qquad (2.2)$$

The constant C has a value of 1.06 if the band pass distribution is assumed rectangular and 0.76 for a Gaussian distribution. Thus, somewhere between 18 and 25 usable fringes can be expected and this agrees very well with the 20 fringes actually obtained.

2.3 End-Wall Alignment

Special care was taken to align the upper light beam of the interferometer with the end wall surface. This was done by making use of the spurious fringes which are formed when slight misalignment occurs (see Appendix A for details). An estimate of the accuracy of this technique shows that the main source of error due to misaligned light rays is actually a result of the finite size light source aperture. For the light source aperture (0.4 mm) collimating lens (71 cm focal length) combination used in these experiments the possible angular deviation of the nominally parallel beam of light is 5×10^{-4} radians. With a 50 mm

test section width this deviation gives rise to a 0.02 mm uncertainty in resolving any point in the boundary layer.

2.4 Focus and Magnification Jig

In order to minimize the errors in the fringe shift pattern due to refraction of light rays, it was necessary to focus the fringes at the 2/3 span of the test section, measured from the entrance window (see Appendix B and Chapter 6 for a detailed analysis). This was accomplished with a carefully machined jig which had two conical tips mounted on it. The separation of the tips was carefully measured on an optical comparator and when the jig was placed in the test section they located the 2/3 span. The film plane was located by placing a bright diffuse light behind the jig and then moving the film holder until these tips were sharply focused. After establishing the film plane the fringes were focused at this plane by suitable adjustment of the MZI plates. Magnification of the test section at the film plane was established from a photograph of the jig with the known separation of the two conical tips.

3. END-WALL THERMAL BOUNDARY LAYER THEORY

Following reflection of the initial shock wave there exists a body of hot stationary gas in contact with a cold wall where both the hot gas and the cold wall can be idealized as semi-infinite in extent. A transition or buffer layer develops between the two, and this layer grows with time. When the shock wave is incident upon the end wall surface, there is a period of a few nanoseconds (at the pressures used here), described by kinetic theory, during which the reflected shock is formed. Subsequently, because of the perturbation to the shock velocity caused by the heat transfer to the wall, there is a transient period before the shock velocity obtains its equilibrium value. It has been shown theoretically[26] and experimentally[12,27] that this latter process requires only a few microseconds. Figure 7 of reference (27) shows that for Mach numbers less than 10 and initial shock tube pressures of 10 Torr the end wall pressure has reached 95% of its ideal value in less than one microsecond.

Neglecting viscous dissipation and assuming constant gas pressure across the boundary layer as a first order approximation the continuity and energy equations can be written as follows:[7]

$$\frac{\partial \rho}{\partial t} + \frac{\partial (\rho v)}{\partial y} = 0 \ , \tag{3.1}$$

$$\rho \frac{\partial h}{\partial t} + \rho v \frac{\partial h}{\partial y} = \frac{\partial}{\partial y} \left(K \frac{\partial T}{\partial y} \right) \ , \tag{3.2}$$

where ρ is the gas density, h the enthalpy per unit mass, y the distance from the wall, v the gas velocity normal to the wall, and K

thermal conductivity. With the aid of the similarity transformation

$$\eta = \left(\frac{\rho_5 c_{p5}}{2K_5 t}\right)^{1/2} \int_0^y \frac{\rho}{\rho_5}\, dy \,, \tag{3.3}$$

and the definition of specific heat at constant pressure c_p, one can transform these equations into a single ordinary differential equation

$$\theta'' + A(T)(\theta')^2 + B(T)\eta\theta' = 0 \,, \tag{3.4}$$

where

$$\theta \equiv \frac{T - T_w}{T_5 - T_w} \,,$$

$$A(T) = (T_5 - T_w)\frac{d}{dt}\left[\ln\left(\frac{K\rho}{K_5\rho_5}\right)\right] \,,$$

$$B(T) = \frac{c_p \rho_5 K_5}{c_{p5}\rho K} \,.$$

Here the subscripts 5 and w refer to the assumed uniform region outside the thermal boundary layer and the conditions at the end wall. The primes in Eq. (3.4) denote differentiation with respect to η.

The boundary conditions are taken as follows:

$$\theta = 0 \qquad \text{at} \quad \eta = 0 \,, \tag{3.5}$$

$$\theta \to 1 \qquad \text{as} \quad \eta \to \infty \,. \tag{3.6}$$

Equation (3.5) expresses the constancy of the wall temperature, while Eq. (3.6) states that the temperature must approach T_5 far from the wall. There is, in fact, some rise in the wall temperature, but it is small for all practical purposes, and will be neglected.

A good first approximation to the thermal conductivity of an un-ionized atomic gas over the temperature range of interest here is

$$\frac{K}{K_w} = \left(\frac{T}{T_w}\right)^{\nu}, \tag{3.7}$$

where ν is a parameter which generally lies between 1/2 (hard sphere interaction) and 1 (Maxwellian particles*), but usually has a value near 3/4. The 3/4 power law gives values of thermal conductivity that are in excellent agreement (within 1% over the temperature range from 1000 to 10000°K) with the theoretical values of Amdur and Mason.[28] Their computations were based on an exp.-6 potential at the lower temperatures and an inverse power potential at higher temperatures. They did not indicate where the transition between the two potentials was made. They did however, indicate that the repulsive exponential potential would be more suitable than the inverse power potential for the higher temperatures. The thermal conductivity was recomputed over the same temperature range for a repulsive exponential potential and the results should be better than the Amdur and Mason values at higher temperatures. Actually these values are 6% lower at 8000°K than the value given by the 3/4 power but converge to Amdur and Mason's results at lower temperatures. This would indicate that ν at the higher temperatures for these experiments should be somewhat lower than the 3/4 value indicated by comparison with Amdur and Mason's results.

Using Eq. (3.7) in Eq. (3.4) one finds:

$$\theta'' + (\nu - 1)\frac{T_5 - T_w}{T}(\theta')^2 + \left(\frac{T_5}{T}\right)^{\nu-1}\eta\theta' = 0 . \tag{3.8}$$

*See page 548 of Ref. 29.

An exact solution of this equation corresponding to $\nu = 1$ is given by

$$\theta = \text{erf}\left(\frac{\eta}{\sqrt{2}}\right) , \tag{3.9}$$

where erf represents the error function.

The differential Eq. (3.8) was rewritten as two first order differential equations in θ and θ'. A value was assumed for θ' at the wall and used in conjunction with the boundary condition $\theta(0) = 0$ to initiate a Kutta-Merson procedure[30] for solving systems of first order differential equations. The integration was continued until θ changed by less than a prescribed value (usually 10^{-5}) with a step in η of 10^{-2}. If $\sqrt{(1-\theta)^2-(\theta')^2}$ * was less than 10^{-3} at this point the integration was terminated. The profile was then transformed back to the physical variables (y,t) with the relation

$$y = \left(\frac{2K_5 t}{\rho_5 c_{p_5}}\right)^{1/2} \left[\frac{T_w}{T_5}\,\eta + \left(1 - \frac{T_w}{T_5}\right)\int_0^\eta \theta\, d\eta\right] . \tag{3.10}$$

The integral here was evaluated with Simpson's rule. In the special case $\nu = 1$, Eq. (3.10) becomes

$$y = \left(\frac{2K_5 t}{\rho_5 c_{p_5}}\right)^{1/2} \left\{\eta + \left(1 - \frac{T_w}{T_5}\right)\left[\sqrt{\frac{2}{\pi}}\left(e^{-\eta^2/2} - 1\right) - \eta\ \text{erfc}\,\frac{\eta}{\sqrt{2}}\right]\right\} , \tag{3.11}$$

where erfc is the complimentary error function.

---

* This error criteria was given by R. R. Nachtsheim and P. Swigert, NASA TN D-3004, (1965).

Equations (3.9) and (3.11) serve as one check on the convergence of the numerical procedure used to solve Eq. (3.8). A second independent check was obtained by comparing the end wall heat transfer rate for all values of ν with a very good approximate analytical solution by Kemp.[31] Agreement for the first check was very good and for the second case the computed heat transfer rates were within 0.5% of the values given by the Kemp formula,

$$\dot{q}_w = 1.13\left[\frac{\rho_5 K_5 c_{p5}}{2t}\right]^{1/2} T_5\left[\frac{1-(T_w/T_5)^{\nu}}{\nu} - \frac{1-(T_w/T_5)^{\nu+1}}{\nu+1}\right]^{1/2} . \quad (3.12)$$

4. EXPERIMENTAL PARAMETERS

The experimental test conditions for this type of study must be chosen very carefully, keeping in mind that for best resolution it is desirable to work with the boundary layer of maximum thickness. For this purpose it is convenient to look at the characteristic thickness δ of the boundary layer given in the similarity parameter of Eq. (3.3) by

$$\delta \alpha \left(\frac{K_5 t}{\rho_5 c_{p5}} \right)^{1/2} . \tag{4.1}$$

From this expression it is clear that one would like to wait for long times after shock reflection (t) and use as low a value for initial pressure (hence low ρ_5) as possible. Usable times after reflection are limited by considerations of shock tube test time and ionization relaxation times. The latter is especially true at the higher temperatures where appreciable ionization can occur behind the reflected shock. At the lower temperatures this is not important because no ionization can occur. Likewise, lower limits for initial pressure are imposed by interferometer sensitivity, which decreases with decreasing density, and non-ideal shock tube behavior that occurs in small tubes operating at low initial pressures.[32,33]

Experiments performed by Dunn[34] in air at the end wall region, under conditions corresponding to the worse case considered in this work, indicate that the uniform slug of hot gas, predicted by ideal theory, persists for at least 400 μ sec after shock reflection. Two time-resolved interferograms were taken in this study, for incident shock Mach numbers of approximately 7, which substantiate this conclusion in that the fringe

spacing is very uniform up to 500 μ sec after shock reflection.

A method for estimating the ionization relaxation time behind the reflected shock (τ_5) is given by Friedman and Fay.[35] By extrapolating the experimental results of Petschek and Byron[36], for relaxation times behind the incident shock, they show that τ_5 scales with p_1 according to

$$p_1\tau_5 = 0.156\ (\frac{\rho_2}{\rho_1})(\frac{\rho_2}{\rho_5})\ \exp(87000/T_5)\ . \qquad (4.2)$$

A plot of $p_1\tau_5$ for initial shock Mach numbers to 10 is shown in Fig. 4. For the experiments used to deduce ν in this work (see Table 3) the typical minimum value of τ_5 is 400 μ sec. This minimum corresponds to an incident shock Mach number of 6.3 into 10 Torr argon. All of the snapshot interferograms in this study (see Table 3) were taken before the onset of ionization.

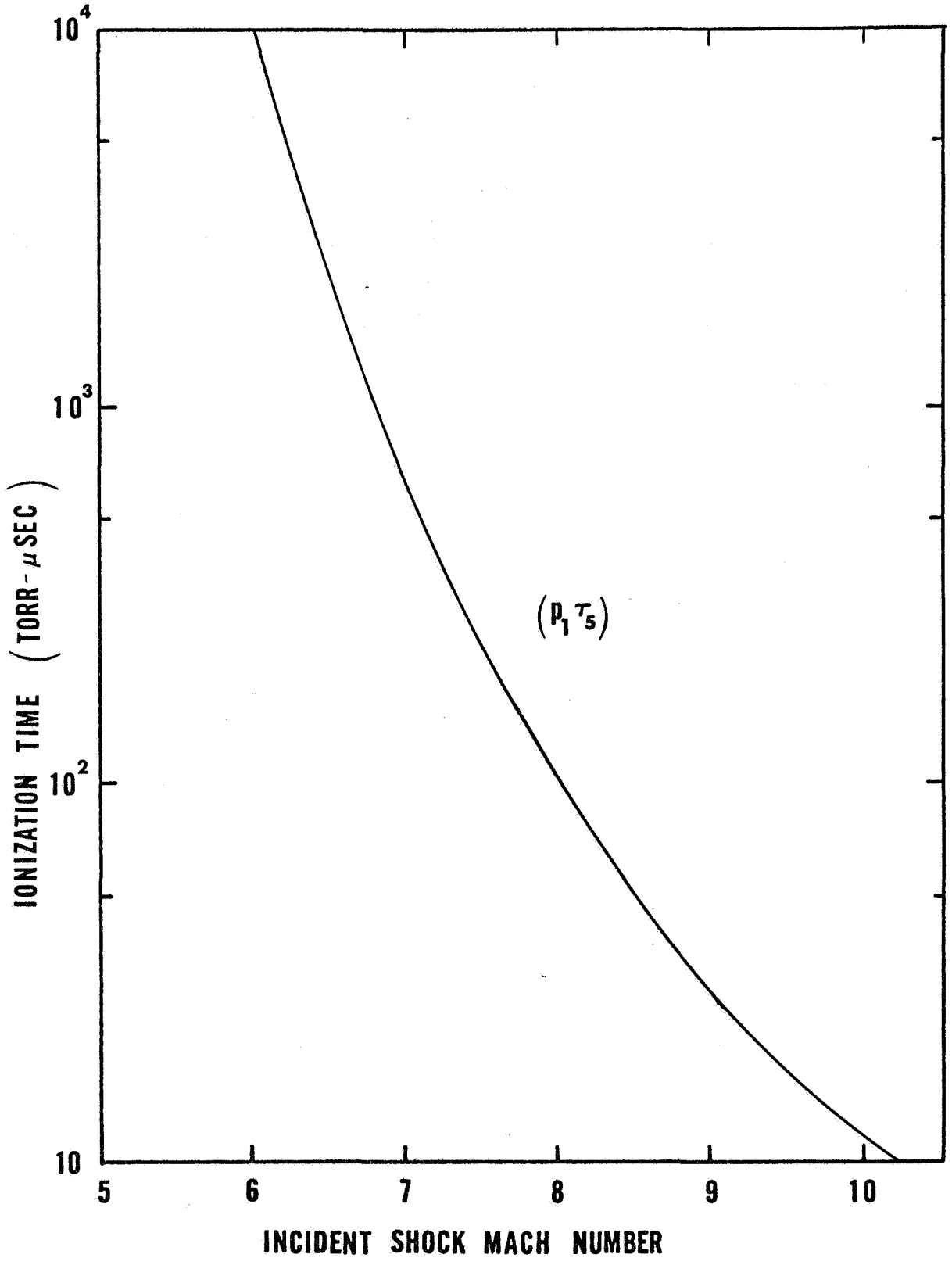

FIG. 4 IONIZATION TIME BEHIND INCIDENT SHOCK IN ARGON

5. EXPERIMENTAL RESULTS

5.1 Interferogram Evaluation

Consider a situation where the refractive index is uniform in both the test section and reference leg of a Mach-Zehnder interferometer. In this case the field of view, as observed at the film plane of a perfect MZI, where the two beams of light make a small angle with each other, will be filled with a band of straight equidistant interference fringes (the so-called wedge fringes). If the refractive index is uniform only in the reference leg, but is a function of the spacial coordinates x, y, z in the test section (see Fig. 5), then the difference in fringe order between (x,y,z) and some reference point in the test section (x_o,y_o,z_o), the so-called fringe shift, is given by[19]

$$S(x,y) = \frac{1}{\lambda}\int_0^{\ell} n(x,y,z)ds - \frac{1}{\lambda}\int_0^{\ell} n(x_o,y_o,z_o)ds \ , \qquad (5.1)$$

where λ is the wavelength of light and the integral is the optical path evaluated for the particular light ray passing through the test section. For an un-ionized gas the refractivity $(n-1)$ is directly related to the density through the Gladstone-Dale constant given by

$$K = \frac{n-1}{\rho} \ , \qquad (5.2)$$

where K is a constant for a given gas and wavelength of light over a wide range of pressures.[37] If the deviation of the light ray from a straight line is not great, then we can replace ds by dz. Equations (5.1) and (5.2) then yield

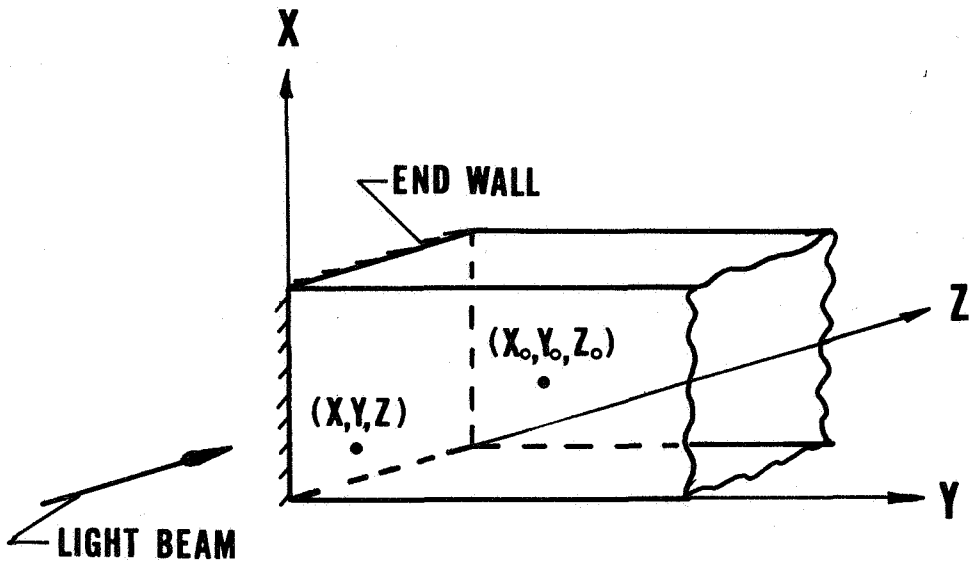

FIG. 5 COORDINATE SYSTEM FOR INTERFEROGRAM EVALUATION.

$$S(x,y) = \frac{K}{\lambda}\left[\int_0^{\ell} \rho(x,y,z)dz - \int_0^{\ell} \rho(x_o,y_o,z_o)dZ_o\right] \tag{5.3}$$

Equation (5.3) is a general integral expression for evaluating the density field from a measured fringe shift distribution. It is implied in writing Eq. (5.3) that all media, except the inhomogeneous test medium, possess constant refractive indices.

Further simplification of Eq. (5.3) is possible if one assumes that the flow field variables depend only on the coordinates (x,y). In this case the basic evaluation equation becomes

$$\rho(x,y) = \frac{\lambda}{K\ell} S(x,y) + \rho_o \ , \tag{5.4}$$

where ρ_o is the known density at (x_o,y_o).

For the case of the end wall boundary layer where the physical variables depend only on y there are two separate considerations which must be made before using Eq. (5.4) to compute the density from the measured fringe shifts. First the gradient of density, and hence refractive index, normal to the light rays may be large enough to curve (refract) them appreciably. If so, the density computed by evaluation of the interferogram on the basis of unrefracted rays will in general be in error. Second, there is a boundary layer which forms on each of the test section windows which can contribute to the measured fringe shift. The first of these problems is considered in detail in Chapter 6 and Appendix B. The general approach to the problem is similar to that of Wachtell[38] where he considered the case of an interferometric analysis of the bounday layer over a flat plate in a supersonic flow. Appendix B is a review of this work. Chapter 6 shows how this analysis can be applied to the end

wall boundary layer problem. The latter problem of the window boundary layer is considered in Appendix C where it is concluded that, for the measurements made in this study the indicated density in the presence of side wall effects is at maximum only 2% different from the true value. This maximum difference occurs for the fringe profile nearest the wall and decreases rapidly for the profiles further from the wall. Thus, no correction was made since it would only effect the last one or two data points on the temperature profile.

5.2 Time Resolved Interferograms

The first series of experiments were conducted, using time-resolved interferometry, with the objective being to establish the thermodynamic state of the gas behind the reflected shock wave. For this purpose the slit of the rotating mirror camera was oriented normal to the end wall and focussed at the camera film plane. A typical record is shown in Fig. 6. Knowing the gas conditions ahead of the incident shock one can compute, using Eq. (5.4), the density in region 2 from the measured fringe shift across the incident shock. In a similar manner one obtains the density behind the reflected shock from the fringe shift across it and the computed density behind the incident shock.

Table 1 is a summary of the results obtained from six such experiments. Listed are the initial conditions (p_1, $T_1 = 298^{\circ}K$) used for the experiments and the measured fringe shifts based on two different assumptions for the flow conditions. The first three columns of the theoretical section are based on the assumption of frozen flow throughout the field and the last three columns are based on the assumption of complete equilibrium. By comparing the measured fringe shifts with the

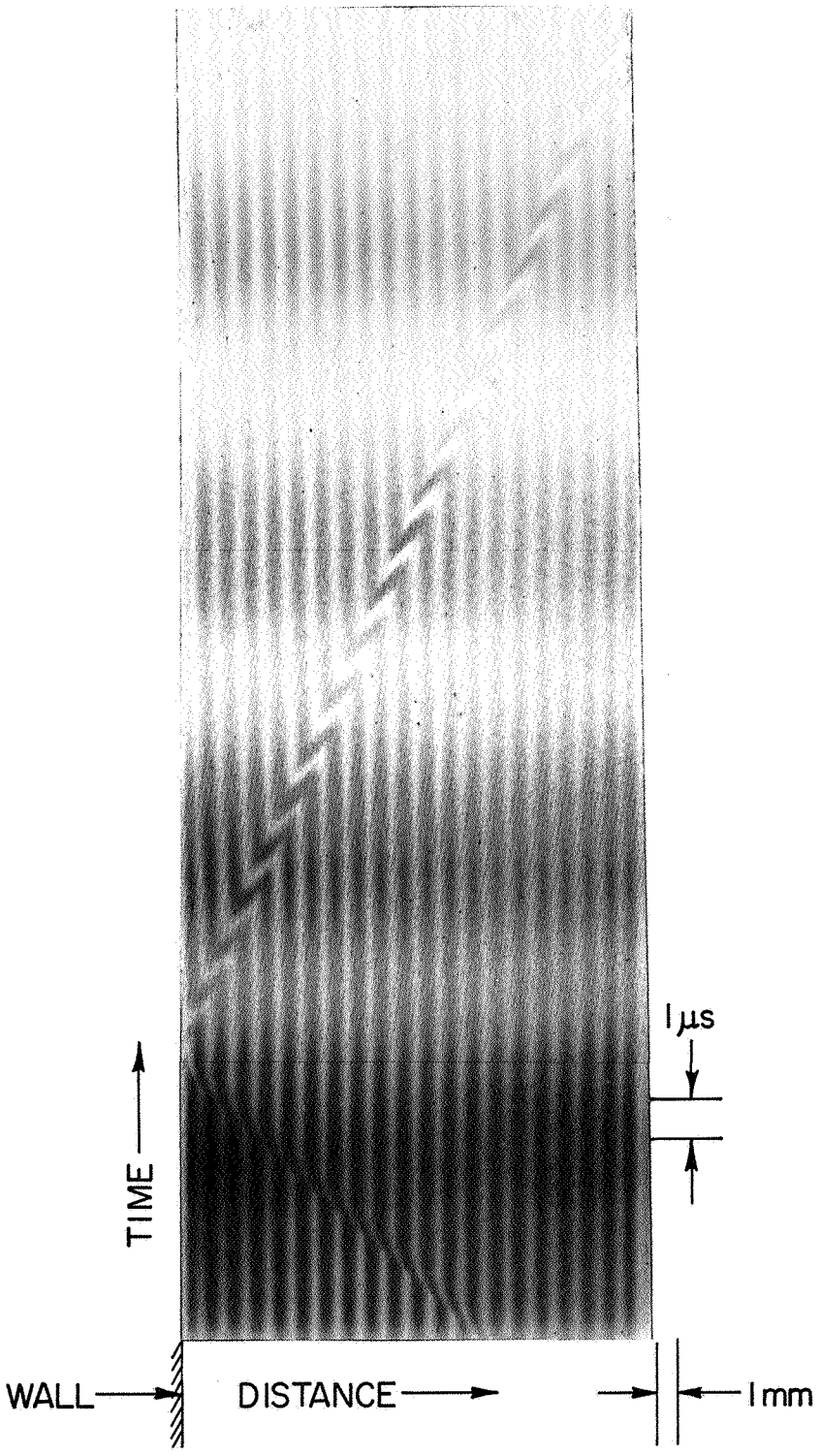

Fig. 6. Time-Resolved Interferogram of End Wall Region ($M = 7.44$, $p_1 = 5$ Torr)

EXPERIMENTAL									THEORETICAL*					
	Pressure Transducer		Recording Film Data						Frozen			Equilibrium		
RUN #	M_I	V_I mm/μs	V_I mm/μs	V_R mm/μs	p_1 Torr	λ Å	S_{12}	S_{25}	S_{12}	S_{25}	V_R mm/μs	S_{12}	S_{25}	V_R mm/μs
62	--	--	2.58	1.02	5	4500	.77▲	1.57▲	.54	1.06	1.32	.54	.81	.98
63	7.37	2.36	2.64	1.37	5	4500	.60▲	1.40▲	.54	1.07	1.36	.54	.76	.98
66	7.44	2.38	2.69	1.02	5	4500	.57	1.44	.54	1.07	1.36	.54	.76	.98
67	7.44	2.38	2.57	0.97	5	5170	.58	1.28▲	.47	0.92	1.30	.47	.60	.99
68	7.37	2.36	2.56	0.99	5	4500	.61	1.33	.54	1.06	1.30	.54	.86	.99
70	7.37	2.36	2.60	1.15	5	4500	.59▲	1.10▲	.54	1.06	1.33	.54	.81	.98

Table 1. Summary of Results for Time Resolved Interferograms

* Computed on basis of V_I as measured on rotating mirror camera film.

▲ Indicates low confidence values due to poor quality fringes.

theoretical values it is clear that the predictions for frozen flow are in better agreement with the experiments than are the predictions for complete equilibrium. This is to be expected because, although some ionization is expected under these test conditions ($\alpha \sim .01$), the time required for ionization relaxation is much longer ($\sim 500\mu$ sec) than the time recorded on the interferogram. It should be pointed out that the agreement between experiment and theory (frozen flow assumption) is not very good in this table. This disagreement was traced to two sources of experimental error. First, the shock velocity V_I was measured using the unreliable pressure transducers and second, the initial pressure p_1 was obtained from an uncalibrated pressure gauge. In all cases the initial shock velocity obtained from the rotating mirror record is greater than the value obtained from the pressure transducers. Figure 7b shows a typical oscillogram of the output from the pressure transducers. From this record it is clear that the signal-to-noise ratio is very low and hence accurate measurements of the shock transit time can not be obtained. The oscillogram in Fig. 7b can be contrasted with the one in Fig. 7a which shows a typical output from a thin film heat transfer gauge. These records are for approximately equal incident shock velocities and it is clear that the thin film gauge must be used here.

The disagreement between the measured and computed fringe shifts in this table is also consistant in the sense that the measured fringe shifts are always greater than the computed values. This would indicate that the initial shock tube pressure was higher than the value indicated by the Wallace and Tiernan. Subsequent calibration of this gauge did indeed show that it was reading approximately 8% low at this pressure.

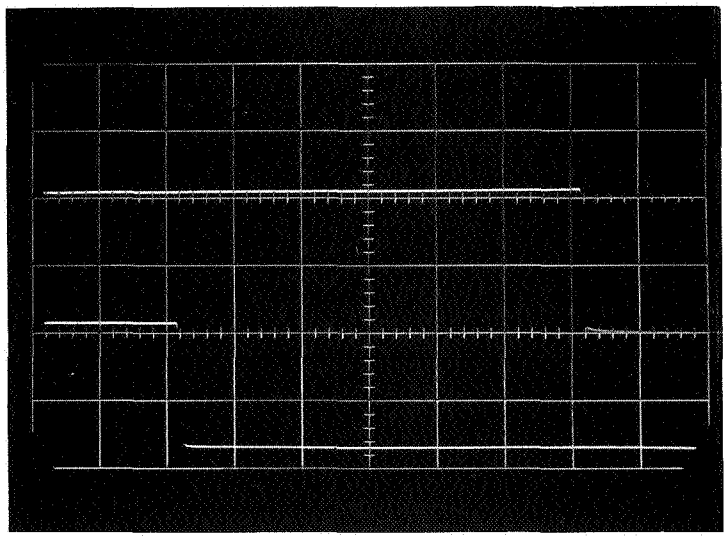

a)

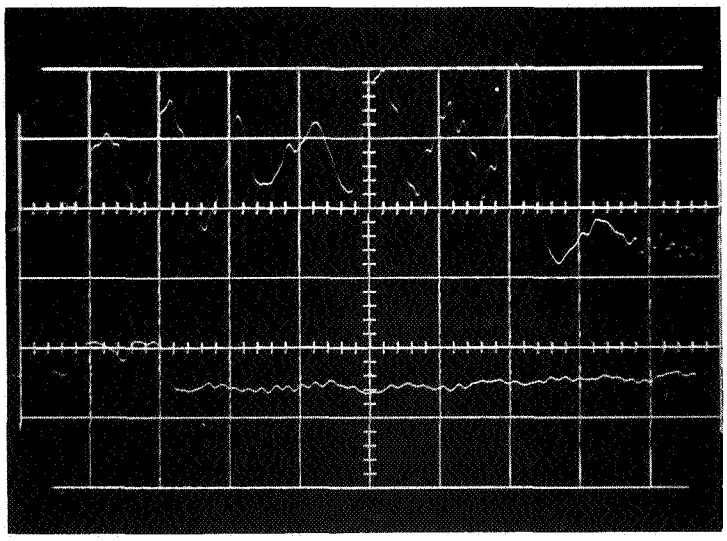

b)

Fig. 7. Typical Oscillogram Records from Shock Detectors.
a) Thin Film Gauges (10 μsec/cm, 2v/cm).
b) Pressure Transducers (10 μs/cm, 20 mv/cm).

When this is taken into account the agreement between theory and experiment is within the experimental uncertainty.

Because of these discrepancies it was considered necessary to make further checks on the state of the gas behind the reflected shock. This was done by taking several snap-shot interferograms of both the reflected and the incident shocks. These tests were conducted using thin film gauges for shock detection and a new (calibrated) Wallace and Tiernan pressure gauge for measuring p_1. Two typical interferograms are shown in Fig. 8. The results from six experiments are shown in Table 2. Two different types of interferograms were necessary in this check because it was not possible, from a monochromatic interferogram, to trace the fringe profile through the reflected shock (see Fig. 8a). That is, one could be in error in reading the fringe shift by an integer number of fringes. To decide the correct value for the integer number of fringes a white-light interferogram (Fig. 8b) was taken where a particular fringe profile can be traced through the shock front. The agreement between experiment and frozen flow calculations as shown in Table 2 is considered very good. On this basis it was concluded that the thermodynamic state of the hot gas behind the reflected shock can be predicted using the simple shock tube relations for an ideal gas.[39] It is further concluded, based on the uniformity of the fringe pattern behind the reflected shock in the time resolved records, that the hot slug of gas in the end wall region is very uniform.

At the beginning of this study it was hoped that the detailed structure of the end wall boundary layer could be obtained from the time-resolved records. In this way it would have been possible to study

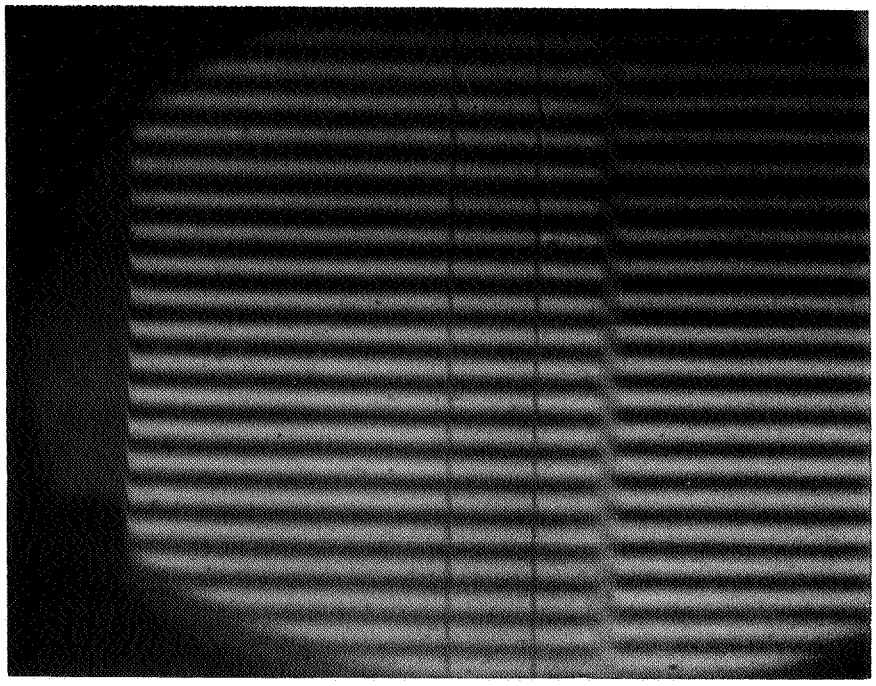

a)

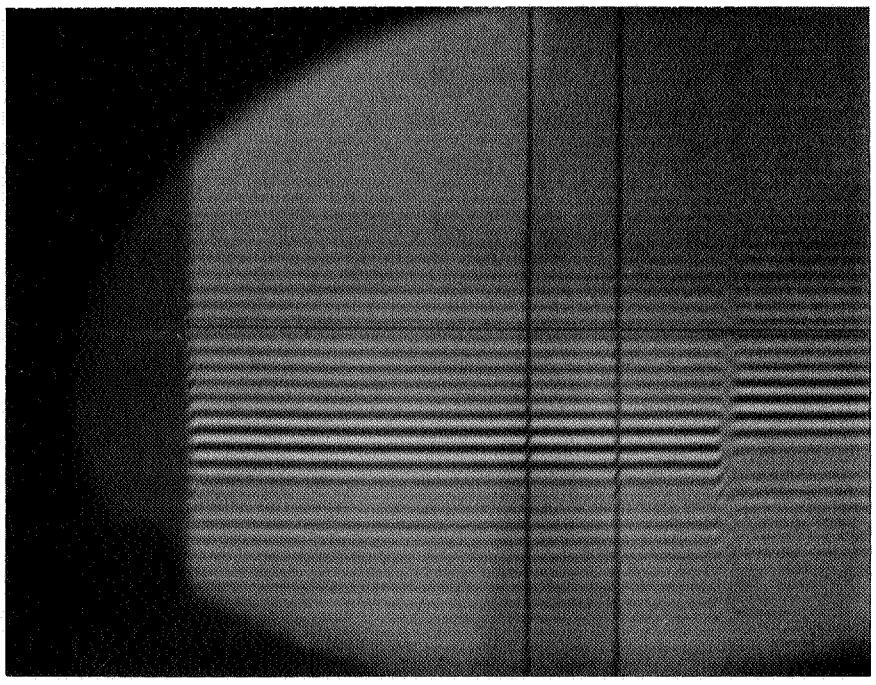

b)

Fig. 8. Typical Snap-Shot Records Showing Reflected Shock.
a) Monochromatic Interferogram (M = 6.62, p_1 = 11 Torr).
b) White-Light Interferogram (M = 6.55, p_1 = 11 Torr).

the growth of the boundary layer profile with time. Unfortunately it was not possible to achieve this goal because of poor resolution of the fringes near the wall. Because of this it was necessary to resort to snap-shot interferograms of the entire end wall region at a particular time after reflection of the initial shock.

Reflected Shock

M_s	p_1 Torr	T_1 ^oK	$S_{25}(\pm.07)$ Experimental	S_{25} Frozen Theory
6.11	10.6	298	1.65	1.696
6.16	10.6	298	1.77	1.693
6.20	10.6	298	1.62	1.697
6.30	10.6	298	1.70	1.709
6.45	10.6	298	1.77	1.721
6.62	10.6	298	1.78	1.726

Incident Shock

M_s	p_1 Torr	T_1 ^oK	S_{12} Experimental	S_{12} Frozen Theory
6.10	10.6	298	0.85	0.869

Table 2. Comparison of Experimental Fringe Shifts with Computed Frozen Flow Fringe Shifts. S_{25} Represents Fringe Shift Across Reflected Shock and S_{12} the Shift Across the Incident Shock.

5.3 Snap-Shot Interferograms

One of the main virtues of using the MZI for boundary layer investigations is the fact that it is easy to change the fringe orientation

and spacing over a very wide range. In this way one can attempt several different fringe orientations and spacings in order to ascertain which gives the most precise resolution for a particular application. In this regard there are several guidelines which have been set by previous investigators studying various types of boundary layers. For example, Howes and Buchele[40] in their investigation of the boundary layer over a flat plate in a supersonic wind tunnel suggest that the most accurate technique is to orient the fringes normal to the surface. In principle this method gives a complete density distribution through the boundary layer because fringes oriented parallel to the gradient in refractive index are shifted in a continuous manner when a continuous change in refractivity occurs. On the other hand, Smeets,[13] in his work at the shock tube end wall, used fringes inclined at approximately 45^{o} to the wall. Bershader and Marlow (in private communication) suggest that very narrow fringes oriented parallel to the wall (and hence normal to the gradient of refractive index) give accurate boundary layer profiles.

In this study a variety of different fringe configurations were used to ascertain the most desirable fringe spacing and orientation for resolving the end wall boundary layer profile. Four typical configurations are shown in Fig. 9. The extent (or thickness) of the thermal layer is readily visible in Figs. 9a,b,c. However, in each of these cases and especially in Fig. 9c it is clear that rapid changes occur in the individual fringe widths as one approaches the wall. Because of this changing fringe width it was not possible to make an accurate determination of the thermal layer profile by fringe shift measurements. For each of the first three cases shown in Fig. 9 different fringe widths were attempted

at the same orientations but here again the above conclusion were still valid.

The final orientation and spacing judged as the one which would give optimum resolution is shown in Fig. 9d. The most striking difference in this record as compared to the previous attempts is that the extent of the boundary layer is not at all clear. Thus, the record which shows the overall effect best is not the one from which the best resolution can be obtained. The initial fringe spacing, for the narrow fringe case, was 4-1/2 fringes per millimeter. The MZI was adjusted such that for an increase in density the fringe shift would be into the field of view. In this way the fringes were compressed in the boundary layer and typically 10 to 12 data points were obtained on a profile less than 2 mm thick. This adjustment of the MZI is critical because if the fringe shift is reversed for the same increase in refractive index the fringes would separate in the boundary layer resulting in only 4 or 5 data points over the 2 mm distance. The 4-1/2 fringes per millimeter spacing represents a practical limitation rather than a desirable one because in principle a much closer spacing would give even more points on a profile. Such a practical limitation is due mainly to the grain structure of the fast response film available. An illustration of this point is shown in Fig. 10. This photograph is an enlargement (mag. $\sim$ 100) of these narrow fringes.

The photograph in Fig. 10 shows that the image of the end wall surface is not well defined in this type of record but it is readily visible in the no flow pictures which were taken prior to each run. In order to establish the location of the wall in the flow record a reference point was established which would be clearly visible in each photograph. Two

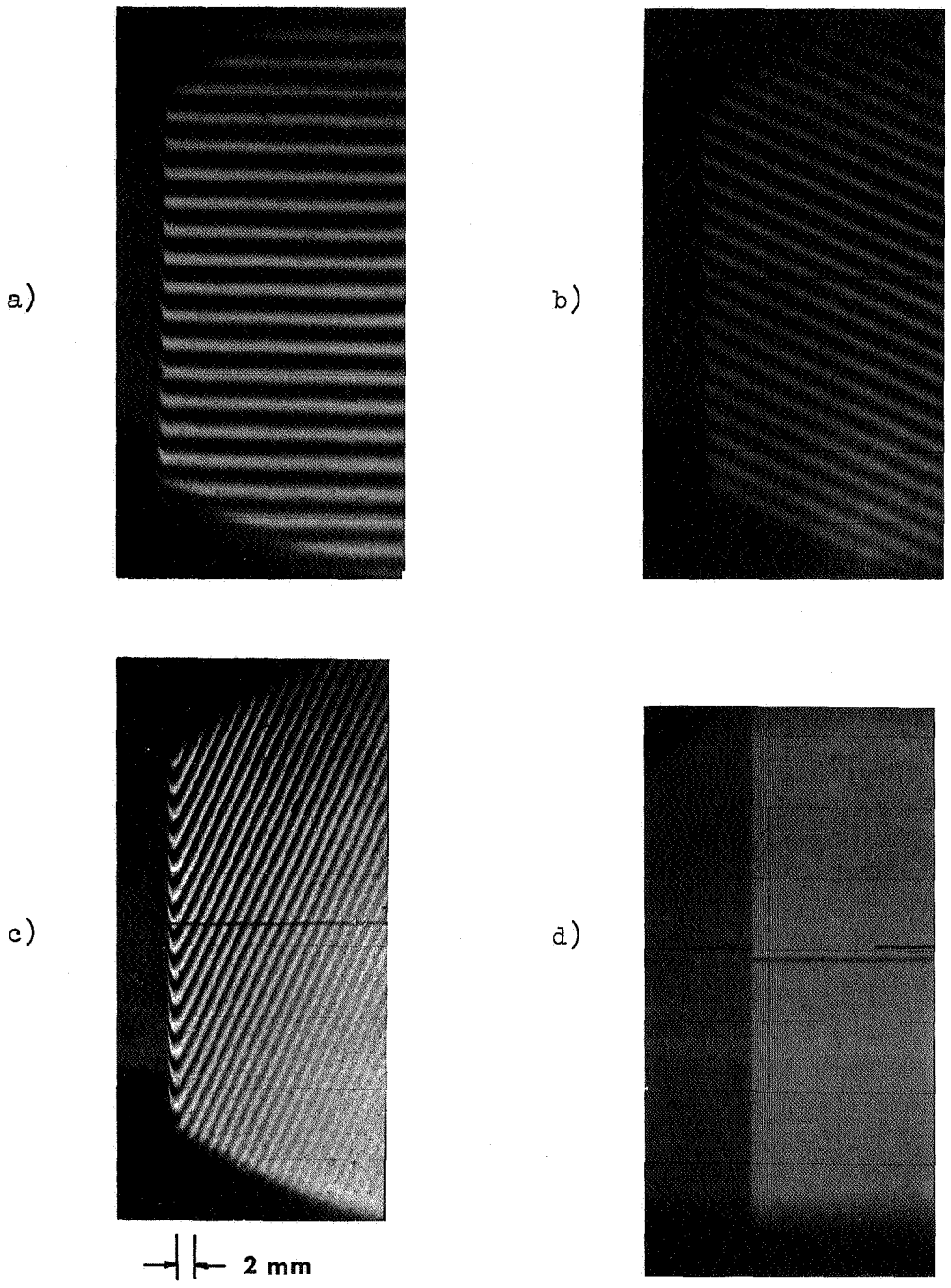

Fig. 9. Four Typical Snap-Shots of the End-Wall Thermal Boundary Layer.

a) Wide Fringes Normal to Surface (M_s = 6.06, p_1 = 11 Torr, t = 22 μsec).
b) Wide Fringes Inclined at 30° to Surface (M_s = 6.21, p_1 = 11 Torr, t = 24 μsec).
c) Wide Fringes Inclined at 65° to Surface (M_s = 6.48, p_1 = 11 Torr, t = 480 μsec).
d) Narrow Fringes Parallel to Surface (M_s = 5.51, p_1 = 11 Torr, t = 488 μsec).

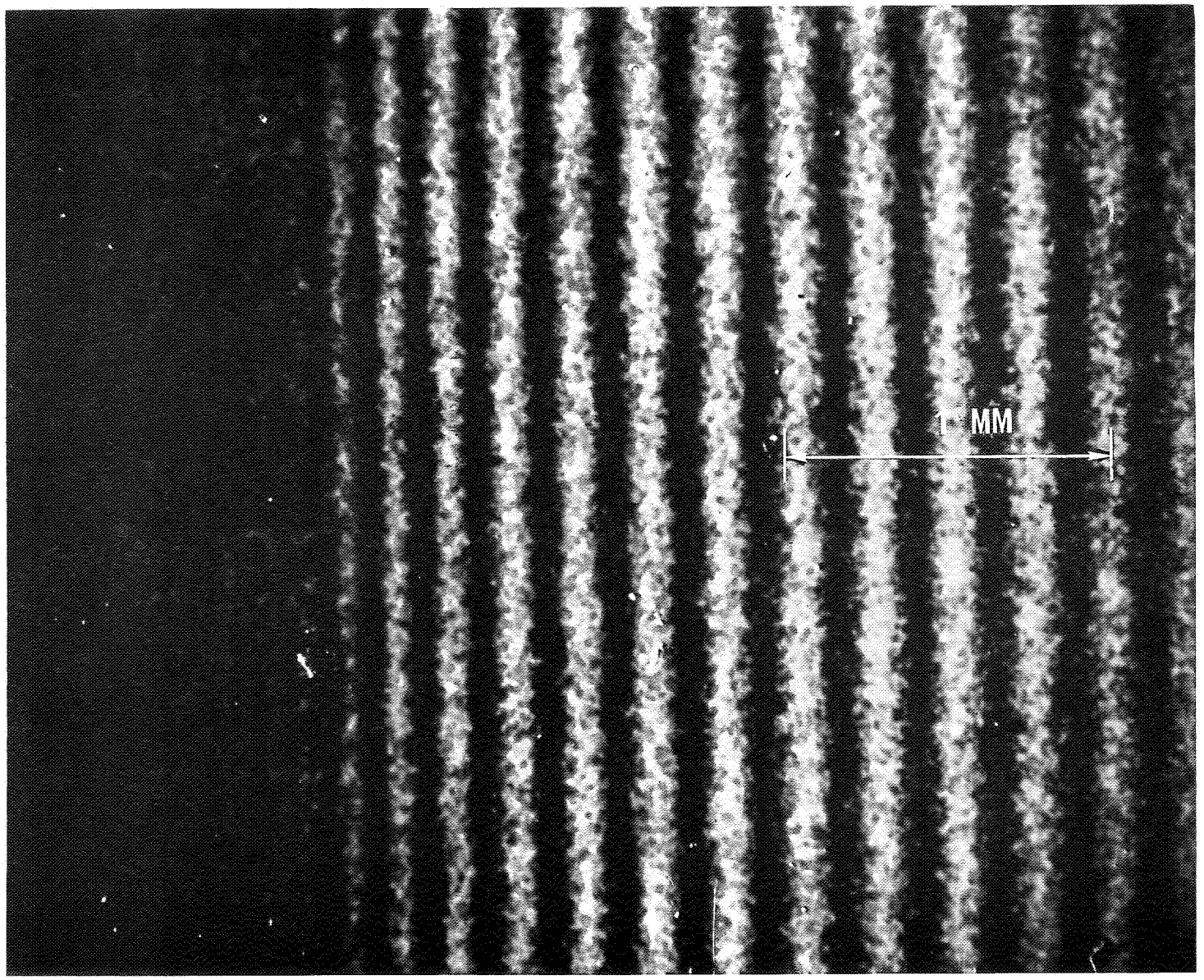

Fig. 10. Enlarged Interferogram of Narrow Fringes Oriented Parallel to the Wall. (M_s = 5.51, p_1 = 11 Torr, t = 488 μsec, Magnification ~ 100).

crossed wires mounted on the window framework served this purpose and all measurements on the flow interferogram were made from this point. With this technique the location of the end wall could be established to within ±0.03 mm. This uncertainty in wall location is the main contribution to the distance error flag which will be presented later.

5.4 Data Reduction Technique

One of the attractive features of using the narrow fringes parallel to the end wall is the relative simplicity of the data reduction process. The procedure consists of measuring in from the reference marks to each fringe maximum and minimum. This distance is then subtracted from the measured wall distance as seen in the no flow record. In this way one obtains the location of each fringe profile relative to the wall. Then, starting at the closest fringe profile to the wall each maximum of light intensity is numbered consecutively $(n = 1,2,3,...)$ and each minimum is likewise assigned one half integrals $(n = 1/2, 1\text{-}1/2, 2\text{-}1/2,...)$. In this way a plot of distance from the wall vs. fringe number gives a convenient means for determining the fringe shift. This numbering system is arbitrary since only the difference in fringe numbers is used to compute the fringe shift.

Figure 11 is a graphical illustration of this technique showing the data for one run. If the flow field were undistrubed the points on a plot of this type would lie on a straight line. However, in the boundary layer the fringes are disturbed and deviate from this line. This deviation, that is, the difference in fringe number from undistrubed position to disturbed position, is the fringe shift corresponding to that particular location. This concept is illustrated in Fig. 11 for a point approximately 1 mm from the end wall.

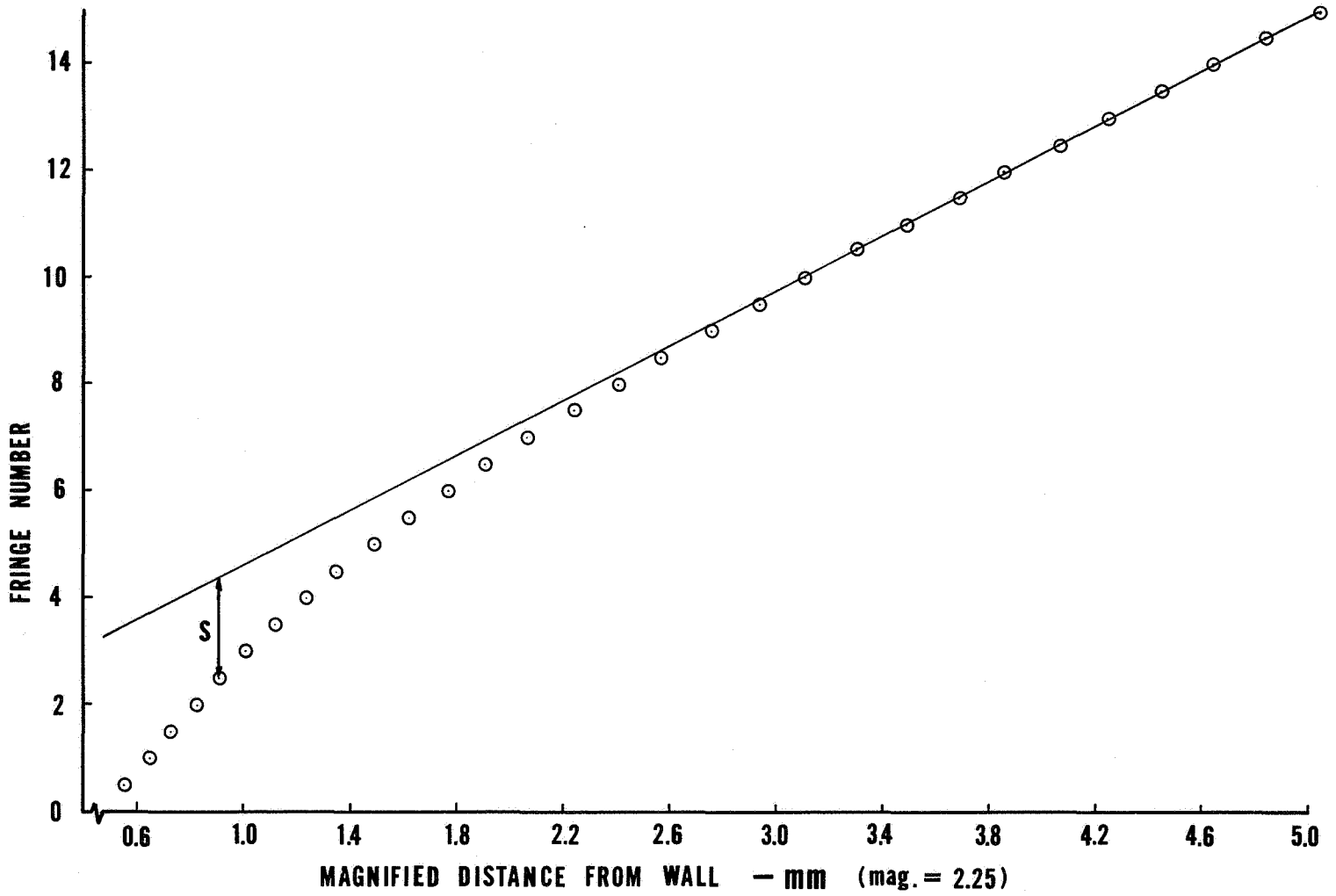

Fig. 11. Schematic of Data Reduction Technique (Data for Run 152).

On a large scale plot of this data it is possible to distinguish those points which lie outside the boundary. Note in Fig. 11 that these points do not lie exactly on a straight line so an averaging process (least squares) was used to establish the undisturbed fringe location. This was done on the computer which then computed the fringe shift for each fringe location in the boundary layer.

Figures 12 and 13 are two examples of normalized temperature profiles obtained in this way. The continuous curves on these plots are for numerical solutions of the thermal boundary layer equation for two different values of ν. As shown in these figures each experimental profile has more than 15 points and in Fig. 12 the last point is 0.2 mm from the wall. Because of refraction of the light rays and other optical problems such as, large grain size of the recording film and excessive "squeezing" of the fringes near the wall it was impossible to measure distinct profiles closer to the wall. The refraction of the light rays of course increases with increasing refractive index gradient (or density gradient) and a consequence of this effect can be seen by comparing Figs. 12 and 13. In Fig. 12 the last visible fringe corresponds to a fringe shift of 2.98 giving a normalized temperature of 0.52. In Fig. 13 the density gradients are much steeper, i.e., the boundary layer is much thinner, and hence the light rays are refracted more. For this case the last visible fringe corresponds to a fringe shift of 1.89 and a normalized temperature of 0.76.

The value of ν which best fits the experimental data was determined by computing the root-mean-square deviation between experiment and theory. Figure 14 shows the mean deviation and the root-mean-square deviation for the data shown in Fig. 12. An uncertainty in ν of $\pm.02$

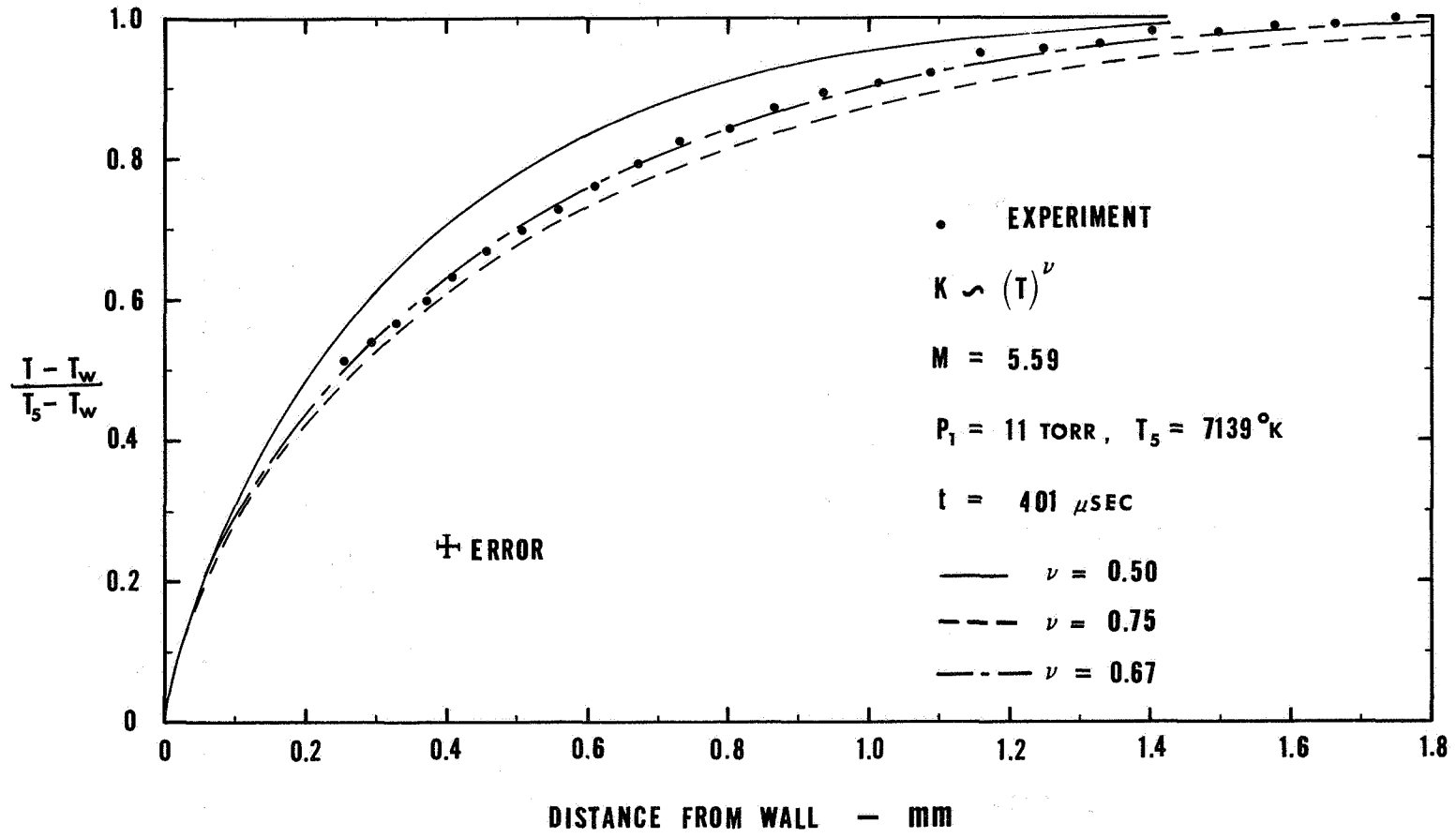

Fig. 12. Normalized Temperature Variation with Distance from Wall for Run 152.

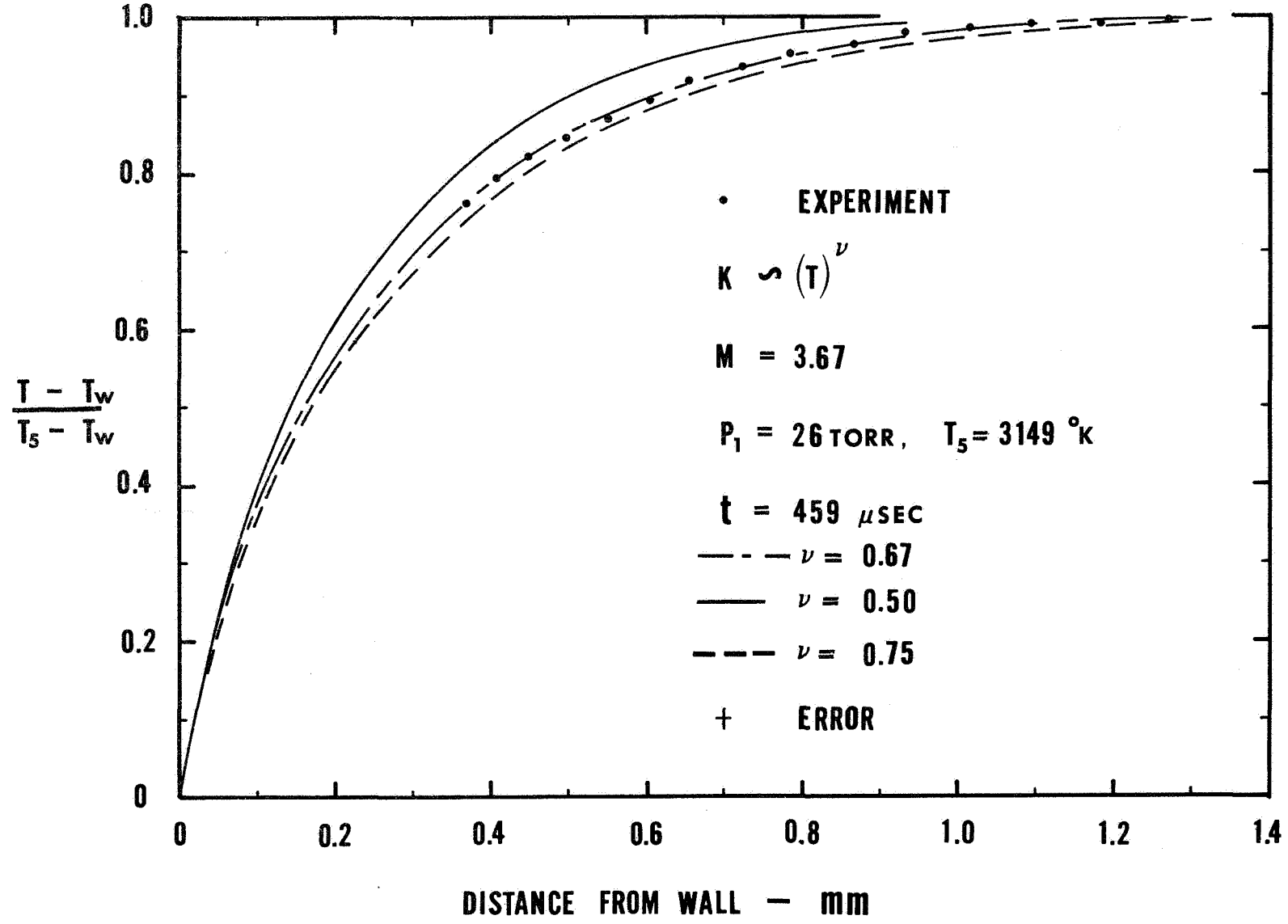

Fig. 13. Normalized Temperature Variation with Distance from Wall for Run 164

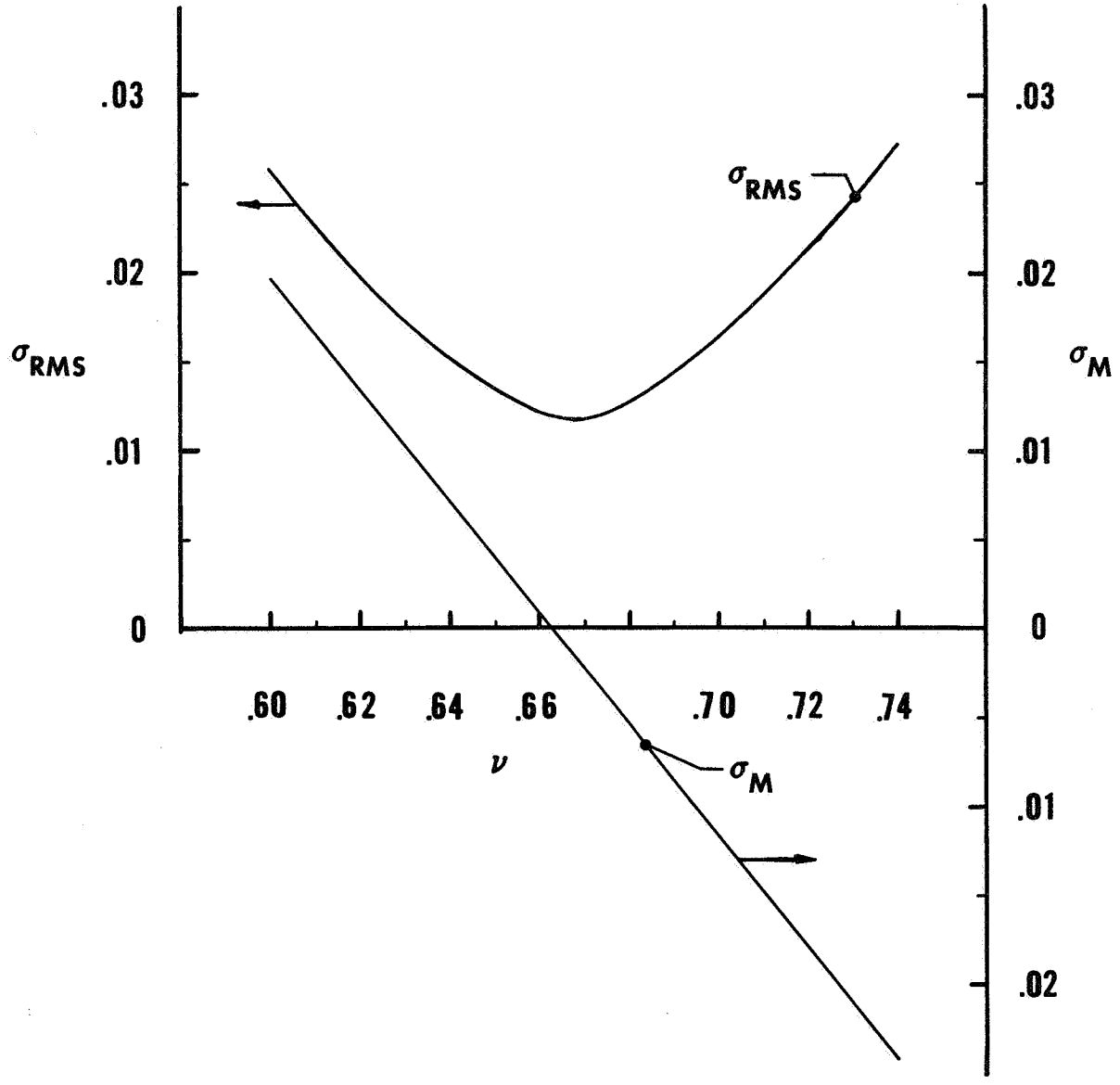

FIG. 14 MEAN AND RMS DEVIATION FOR RUN 152

was assigned on the basis of the error flags shown in Figs. 12 and 13. That is, for the data shown in Fig. 12 a value of 0.65 for ν is a lower limit which encloses the error flag and a ν of 0.69 is a upper limit which encloses the error flag. Table 3 is a summary of the results for nineteen runs showing the experimental parameters and the value of ν as established by this technique.

Run	M_s	p_1 TORR	T_s ^oK	t μsec	ν
164	3.67	26	3149	459	.67
162	3.67	31.2	3149	369	.66
163	3.89	20.8	3522	383	.65
161	4.18	20.8	4050	409	.65
160	4.37	20.8	4409	422	.66
159	4.63	20.8	4933	227	.72
156	4.68	20.8	5049	330	.66
155	4.92	20.8	5558	502	.65
154	5.25	20.8	6315	488	.66
153	5.44	20.8	6754	265	.67
149	5.51	20.8	6943	488	.65
150	5.55	20.8	7040	510	.64
152	5.59	20.8	7139	402	.67
146	5.93	20.8	8020	389	.66
145	6.17	20.8	8658	401	.64
144	6.27	20.8	8934	395	.65
157	6.32	20.8	9078	396	.67
143	6.37	20.8	9225	398	.70
166	7.27	5.8	11949	21	.70

Table 3. Summary of Basic Experimental Data and Calculated Results

6. REFRACTIVE ERROR ANALYSIS

When the MZI is used for studying regions where there are large density gradients, it is necessary to consider the possibility of an error in the measured fringe shift which occurs as a result of refraction of the light rays. That is, the gradient in density will cause a light ray to bend in the direction of increasing density and hence follow a curved path through the test section rather than the straight path which is assumed in simple interferometer theory. This phenomenon results in two main effects: First each ray will travel over a longer optical path and along this path the refractive index (and hence density) is constantly changing. Second the location of the fringe profile with respect to the end wall may be distorted because the ray does not actually pass through the point from which it appears to originate. Thus, an interferogram evaluated on the basis of unrefracted light rays will in general be in error.

The object of this section is to apply the results of a general method for computing refractive errors to the specific problem of light refraction within the end wall thermal boundary layer. The general problem of refraction has been treated for the case of supersonic flow over a flat plate for wind tunnel applications by several authors including Blue[41], Bershader[42], Weyl[43], DeFrate[44], Wachtell[38], and Howes and Buchele.[40,45-47] The method to be utilized here was first derived by Wachtell[38] and a complete review of his analysis is given in Appendix B. The work of the first four authors was completed just prior to Wachtell's and in an appendix he compares their results with his own conclusions. Howes and Buchele's work was completed subsequent to that of Wachtell and the last reference listed for these authors is

a very recent summary and extension of their work which was substantially completed prior to 1955. In Appendix B the general results of Wachtell, expressed as a power series expansion, are compared with two limiting cases presented, for the more general integral formulation of the problem, by Howes and Buchele.[47] It is shown that for these two specific cases the different formulations are identical. Unfortunately, the most general expression for refractive error correction of Ref. 47 is not in a form convenient for comparison with the full Wachtell series expansion.

Another completely different method for evaluating refractive errors was given in DeFrate.[44] Basically his approach is to assume a density distribution and with this numerically integrate the differential equation for the trajectory of a light ray (see Eq. (B.7)). Once the trajectory, corresponding to an assumed density distribution, is known, the expected fringe shift, including the effects of refraction, can be computed. Thus, the DeFrate procedure is to guess the true density distribution, compute for this guess what the measured fringe shift distribution should be, and compare it with the fringe shifts actually measured. A new guess will be suggested by any discrepancy and this process is repeated until good agreement is obtained. The advantage of this procedure as compared to the Wachtell method is that it appears to be valid when the Wachtell approach breaks down because of lack of convergence of the power series expansion. This iterative approach is not used here primarily because it does not show explicitly how to minimize refractive errors and also because it involves the numerical solution of a differential equation while the Wachtell method gives the solution in a power series expansion. Another important reason for using the Wachtell method is that

it separates the refractive error and the distortion effects from the main fringe shift contribution attributed to the density field being studied. DeFrete's method does not consider the effects separately but rather incorporates the entire problem into the iterative scheme.

The problem of refractive errors for supersonic flow over a flat plate in the wind tunnel is somewhat different from the present case. There the density increases toward the free stream causing a particular light ray to bend away from the plate, whereas, for the thermal boundary layer, the density increases near the wall causing the rays to bend toward the wall. This difference is a fundamental one because each entrance ray that bends sufficiently to hit the end wall surface is lost for purposes of forming interference fringes. That is, a "blind" region will exist near the wall. The extent of the region will be at least as large as the distance from the wall out to the first entrance ray which just hits the edge of the surface. Most likely this blind area will extend even further because of interference between the rays that re-reflect from the surface and those which do not hit the surface but nevertheless are still refracted appreciably.

In order to evaluate the coefficients for the power series expansion for refractive error fringe shift contribution given by Eq. (B.20) one must first express b_1, b_2, and b_3 in terms of the parameters of the thermal boundary layer. Equations (B.21), (B.22), and (B.23) give expressions for the first three b_i coefficients in terms of density gradients evaluated at the entrance station of the particular light ray under consideration. These gradients can be expressed in terms of the thermal boundary layer parameters by defining a non-dimensional function of density $f(\eta)$ as

$$f(\eta) = \frac{\rho_w - \rho(\eta)}{\rho_w - \rho_5} \tag{6.1}$$

where η is the similarity parameter given in Eq. (3.3). From the definition of θ given in Eq. (3.4) it can be shown that

$$f(\eta) = \frac{\rho(\eta)}{\rho_5}\,\theta(\eta) \ .$$

Now using the chain rule of differentiation one obtains

$$b_1 = C^2\,\frac{\delta}{D^2}\,\frac{T_w T_5}{T_E^3}\,\theta_E' \ , \tag{6.2}$$

$$b_2 = \frac{C^2}{2D^2}\,\frac{T_w T_5^3}{T_E^4}\left[(\nu+2)\left(\frac{T_5-T_w}{T_E}\right)(\theta_E')^2 + \left(\frac{T_E}{T_5}\right)^{1-\nu}\eta\theta_E'\right] \ , \tag{6.3}$$

and

$$b_3 = \frac{C^2}{6}\,\frac{1}{D^2\delta}\,\frac{T_w T_5^4}{T_E^5}\,\theta_E'\left\{(2\nu^2+7\nu+6)\left(\frac{T_5-T_w}{T_E}\right)^2(\theta_E')^2\right.$$

$$(3\nu+7)\left(\frac{T_5-T_w}{T_E}\right)\left(\frac{T_E}{T_5}\right)^{1-\nu}\eta\theta_E' + \left[\left(\frac{T_E}{T_5}\right)^{1-\nu}\eta^2 - \eta(1-\nu)\left(\frac{T_5-T_w}{T_E}\right)\theta_E'\right.$$

$$\left.\left.-1\right]\left(\frac{T_E}{T_5}\right)^{1-\nu}\right\} \tag{6.4}$$

where the subscript E denotes values at the entrance station of the light ray and C and δ are defined as

$$C = D\left(\frac{\rho_5 c_{p5}}{2K_5 t}\right)^{1/2}\sqrt{K(\rho_w-\rho_5)} \ , \tag{6.5}$$

and

$$\delta^2 = \frac{2K_5 t}{\rho_5 c_{p5}} \tag{6.6}$$

In writing the expressions for b_2 and b_3 the governing equation for the thermal boundary layer, Eq. (3.8), was used to express the higher order derivatives of θ in terms of the first order derivative θ'. The nondimensional parameter C defined by Eq. (6.5) represents the ratio of the test section width to the thermal boundary layer thickness multiplied by the square root of the total change in refractive index from region 5 to the wall.

If one now defines a new nondimensional density

$$\bar{f}(\eta) = \frac{\rho_w - \rho(\eta)_{MEAS}}{\rho_w - \rho_5} \tag{6.7}$$

where $\rho(\eta)_{MEAS}$ is the value of density computed from the interferogram, then the difference between f (see Eq. (6.1)) and $\bar{f}$ will be given by

$$\delta f = f - \bar{f} = \frac{\rho_{MEAS} - \rho}{\rho_w - \rho_5} = \frac{\delta\rho}{\rho_w - \rho_5} \tag{6.8}$$

where ρ denotes the true value of density. Now this difference in measured and true density $\delta\rho$ is due to the refractive error and one can write

$$\delta f = \frac{\lambda S_R}{KD} \frac{1}{(\rho_w - \rho_5)} \tag{6.9}$$

where S_R is the additional fringe shift due to refraction as given by the power series expansion in Eq. (B.20). Considering, for simplicity, only the first two terms in the power series for λS_R one can write

$$\lambda S_R = \frac{b_1^2}{2} D^3 \left\{ \left(\frac{\alpha}{2} - \frac{1}{6} \right) + \left[\frac{b_1^2}{8} - b_2 \alpha^2 + b_2 \alpha + \frac{b_1^2}{40} \right.\right.$$

$$\left.\left. - \frac{b_2}{5} - \frac{b_1^2 \beta}{8} \left(\frac{1}{\eta_g^2} - 1 \right) \right] D^2 \right\} \qquad (6.10)$$

In this expression α is a parameter which defines the focal plane for the fringes in the test section and β is a parameter containing the thickness and refractive index of the test section exit window. From this form of the equation one can conclude that to first order the contribution of refractive errors will be zero if $\alpha = 1/3$. This value of α corresponds to a focal plane loacted at 2/3 the test section span measured from the entrance window. This conclusion was also drawn by Wachtell[38] and is, in fact, independent of the particular problem under consideration. This conclusion is the single most important point of this analysis and all of the interferograms taken in this study were for fringes focussed at this plane.

There are some further general conclusions which can be drawn from Eq. (6.10) and to see this one must inspect the order of magnitude of the b_i coefficients given for the thermal boundary layer by Eqs. (6.2), (6.3) and (6.4). Consider first the ratio of b_1^2 to b_2 which can be written as:

$$\frac{b_1^2}{b_2} = 2 \left(\frac{\delta}{D} \right)^2 C^2 \frac{T_w T_5}{T_E^2} \theta_E' \left[(\nu + 2) \frac{T_5 - T_w}{T_E} \theta_E' + \left(\frac{T_E}{T_5} \right)^{1-\nu} \eta \right]^{-1} . \qquad (6.11)$$

The limits of this expression can be determined by considering three separate points in the boundary layer corresponding respectively to the

outer edge where $\theta = 1$, a point midway on the non-dimensional termperature profile where $\theta = 1/2$, and a point at the end wall where $\theta = 0$. Consider first the limit at the outer edge of the boundary layer where $\theta \to 1$. For this condition $T_E \to T_5$, $\theta_E' \to 0$, and $\eta \to 4$. The above condition on T_E is obvious and the conditions on θ_E' and η are obtained from the numerical solution of the governing differential equation given by Eq. (3.8). Thus in the limit $\theta \to 1$ the expression given in Eq. (6.11) becomes

$$\lim_{\theta \to 1} \frac{b_1^2}{b_2} = 2 \left(\frac{\delta}{D}\right)^2 C^2 \frac{T_w}{T_5} \frac{\theta_E'}{\eta} \quad . \tag{6.12}$$

Next consider the limit as $\theta \to 0$. For this case $T_E \to T_w$, $\eta \to 0$, and θ_E' is a number less than $1/2$. Again the conditions on T_E and η are obvious and the result stated for θ_E' was observed for the numerical solution of the governing differential equation. Under these conditions the limit of Eq. (6.11) becomes

$$\lim_{\theta \to 0} \frac{b_1^2}{b_2} = 2 \left(\frac{\delta}{D}\right)^2 \frac{c^2}{\nu + 2} \quad . \tag{6.13}$$

Now finally consider the mid point for $\theta = 1/2$. For this case $\theta_E' \sim 1/2$ and $\eta \sim 2$. Both of these conditions are again obtained from the numerical solution for typical conditions used in this work. In order to find the maximum limit one must find the minimum limit for the bracket term in Eq. (6.11). Noting that the ratio θ_E'/θ is of order unity the minimum value of the bracket term becomes

$$(\nu + 2)\left(\frac{T_5}{T_E} - 1\right) + \eta$$

This quantity is greater than unity and does not go to zero hence one can write

$$\lim_{\theta \to 1/2} \frac{b_1^2}{b_2} = 2\left(\frac{\delta}{D}\right)^2 C^2 \theta_E' \frac{T_w T_5}{T_E^2} \frac{1}{\left[(\nu+2)\left(\frac{T_5}{T_E} - 1\right)\right] + \eta} \quad . \tag{6.14}$$

From the three cases one can now write a conservative condition for which b_1^2 will always be much less than b_2. This condition is given by

$$\left(\frac{\delta}{D}\right)^2 C^2 \theta_E' \ll 1 \quad . \tag{6.15}$$

In this same way one can also show that if the above condition is true the

$$b_1^3 \ll b_3 \quad , \tag{6.16}$$

and

$$b_1 b_2 \ll b_3 \quad . \tag{6.17}$$

As a guide in choosing experimental parameters Fig. 15 shows values of C computed for different values of initial pressure (p_1), time after reflection (t), and exponent in the power law dependence for thermal conductivity ν (see Eq. (3.7)). Figure 13a shows the variation of C with temperature at the outer edge of the boundary layer (T_5) for various times after reflection and two different initial pressures while holding ν fixed at its minimum value of 1/2 (see Sec. 3). Likewise, Fig. 15b shows the variation of C with T_5 at a fixed time after reflection (400 μ sec) and different initial pressure and ν's. In order for the condition given by Eq. (6.15) to be satisfied, and indeed

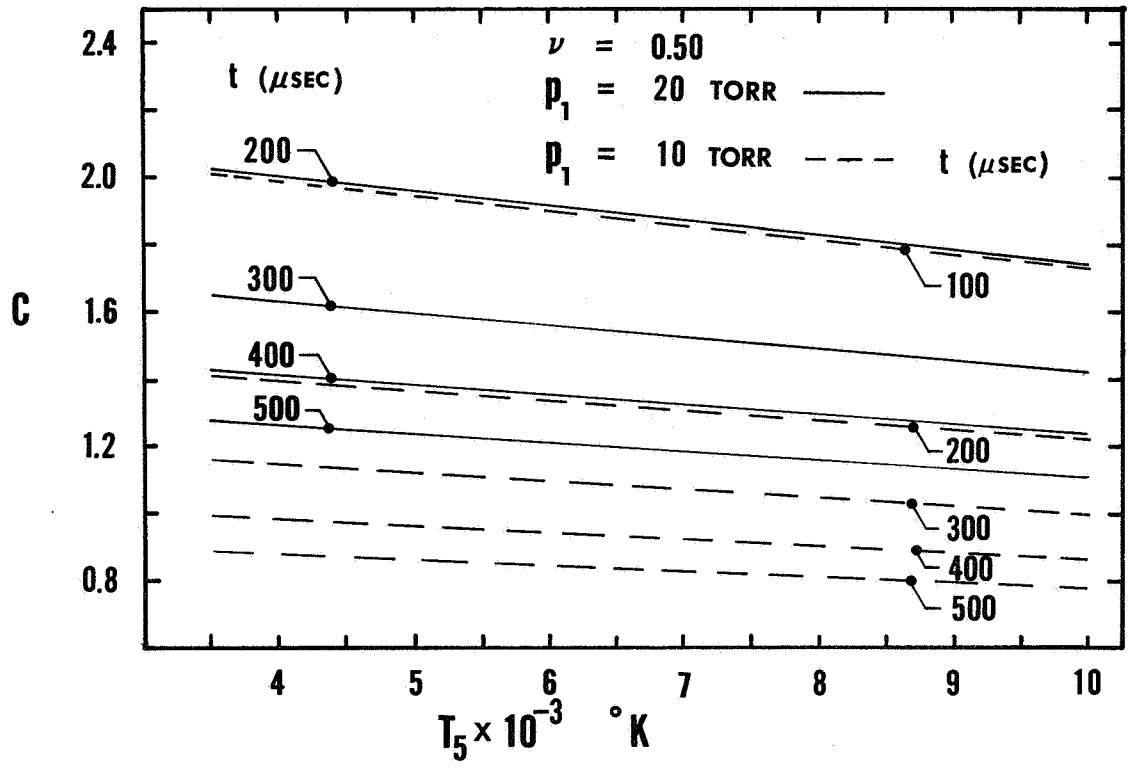

(a)

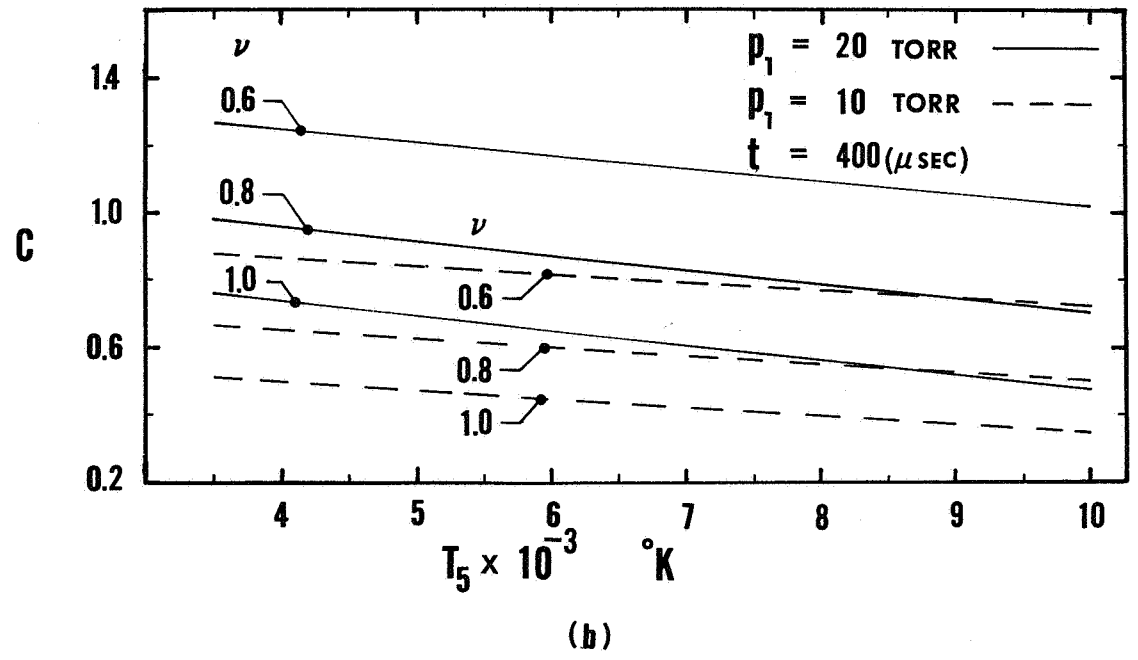

(b)

Fig. 15. Variation of C with Temperature in Region 5.

in order to have minimum refractive errors as will be shown later, one should choose experimental parameters that give minimum C if at all possible. The choice of such parameters to give minimum C (viz. low p_1 and long time after reflection) is consistent with the discussion of Sec. 4 where the same conclusions were drawn for completely different reasons.

It is now possible, assuming experimental conditions consistent with Eq. (6.15), to simplify the expression for λS_R by neglecting the lower order terms indicated by the order of magnitude analysis for the b_i coefficients. Doing this the complete expression given by Eq. (B.20) becomes

$$\lambda S_R = b_1^2 D^3 \left\{ \left(\frac{\alpha}{2} - \frac{1}{6} \right) + \left[\left(-\alpha^2 + \alpha - \frac{1}{5}\right) b_2 \right] D^2 \right.$$

$$+ \left[\left(\alpha^3 - \frac{3\alpha^2}{2} + \frac{3\alpha}{4} - \frac{3}{28}\right) b_1 b_3 \right.$$

$$\left. \left. + \left(-\frac{2}{3}\alpha^2 + \frac{4\alpha}{9} - \frac{4}{63} \right) b_2^2 \right] D^4 + \text{---} \right\} \qquad (6.18)$$

where β no longer appears as a parameter. This means that the exit window has no influence, at least to this order, on the refractive error contribution. This conclusion is consistent with the findings of both Wachtell[38] and Howes and Buchele.[47]

As was mentioned previously α was taken as 1/3 in this study in order to eliminate the first order contribution to S_R and for this choice the next two higher order terms of Eq. (6.18) become:

$$\lambda S_R = b_1^2 D^3 \left\{ \left(\frac{b_2}{45} \right) D^2 + \left(\frac{b_1 b_3}{10} + \frac{2 b_2^2}{189} \right) D^4 \right\} . \qquad (6.19)$$

Written in this form one can now see that the choice $\alpha = 1/3$ while eliminating the first order contribution to S_R also gives reasonably small

coefficients for the remaining higher order contributions. In principle one could choose α such that the entire three term expansion given by Eq. (B.20) would be minimized. No attempt was made to do so here.

Equation (6.19) can also be written in terms of the non-dimensional constant C by substitution of the expressions for the b_i coefficients given in Eqs. (6.2), (6.3), and (6.4). Doing this and after some simplification one finds

$$\lambda S_R = \frac{\delta^2}{D} \frac{T_w^3 T_5^7}{T_E^{10}} \left\{ \frac{P}{90} \bar{C}_E^3 + \right.$$

$$\left. \frac{T_w T_5^3}{T_E^4} \left[\frac{Q}{60} + \frac{P^2}{378} \right] \bar{C}_E^4 + \cdots \right\} \tag{6.20}$$

where

$$P \equiv (\nu + 2) \left(\frac{T_5 - T_w}{T_E} \right) \theta'_E + \left(\frac{T_E}{T_5} \right)^{1-\nu} \eta, \tag{6.21}$$

$$Q \equiv (2\nu^2 + 7\nu + 6) \left(\frac{T_5 - T_w}{T_E} \right)^2 (\theta'_E)^2 +$$

$$(3\nu + 7) \left(\frac{T_5 - T_w}{T_E} \right) \left(\frac{T_E}{T_5} \right)^{1-\nu} \eta \, \theta'_E +$$

$$\left[\left(\frac{T_E}{T_5} \right)^{1-\nu} \eta^2 - \eta(1-\nu) \left(\frac{T_5 - T_w}{T_E} \right) \theta_E - 1 \right] \left(\frac{T_E}{T_5} \right)^{1-\nu}, \tag{6.22}$$

and

$$\bar{C}_E \equiv C^2 \theta'_E \tag{6.23}$$

Thus we see that for fringes focused at the 2/3 span of the test section and under experimental conditions such that Eq. (6.15) is satisfied one can express the refractive errors as a power series in the non-dimensional parameter $\bar{C}$. For completeness the non-dimensional change in density (δf) given by Eq. (6.9) will now be expressed as a power series in $\bar{C}_E$. Doing this one finds

$$\delta f = \frac{T_w^3 T_5^7}{T_E^{10}} \theta_E' \left\{ \frac{P}{90} \bar{C}_E^2 + \frac{T_w T_5^3}{T_E^4} \left[\frac{Q}{60} + \frac{P^2}{378} \right] \bar{C}_E^3 + \text{---} \right\} \qquad (6.24)$$

where P and Q are defined by Eqs. (6.21) and (6.22).

In summary it has been shown that the refractive error contribution to fringe shift (S_R) for the thermal boundary layer problem can be expressed as a power series in $\bar{C}_E$. The form this power series takes in Eq. (6.20) assumes only that the interference fringes are focused at the 2/3 span of the test section and that the experimental parameters are chosen such that Eq. (6.15) is satisfied. This power series was then used to express δf in terms of the parameters of the thermal boundary layer and here it turned out that the terms in the power series for δf were one order lower in $\bar{C}_E$ than the terms in the expansion for S_R. The non-dimensional grouping given by $\bar{C}_E$, which appears naturally in the derivation of Eqs. (6.20) and (6.24), at first does not seem like a wise choice for the power series expansion parameter because as the subscript E indicates it is dependent on the distance from the wall. However, this choice is preferable over the other alternative available (viz. C) because as Fig. 15 clearly demonstrates C can be greater than unity for the particular parameters used in this study. It is also clear from Fig. 15

that C is no larger than 2 and experience with the numerical solution of the full thermal boundary layer equation shows that θ_E' is always less than 1/2. Thus it is reasonable to conclude that $\bar{C}_E$ is a better parameter for the power series expansion of the thermal boundary layer refractive error than the more satisfying choice C.

Returning now to a consideration of only the refractive error fringe shift S_R it is clear from the leading coefficient of Eq. (6.20) that S_R increases with decreasing T_E. Not only does the leading term increase as the wall is approached but also $\bar{C}_E$ increases due to the increase in θ_E'. At the outer edge of the boundary layer where $T_E \to T_5$ and $\bar{C}_E \to 0$ the value of S_R must approach zero. This is consistent with the physical situation where the density gradients at the outer edge of the boundary layer are very small hence the light refraction should be negligible; as the density gradients increase further into the boundary layer the refraction increases and hence the refractive error increases.

The above conclusions can best be demonstrated from an illustrative example where second and third order contributions (first order is zero for $\alpha = 1/3$) to S_R are computed for a typical example. This has been done for the experimental parameters of run 152 (data shown in Fig. 12) using the value of ν obtained from the method described in Section 5. Table 4 is a list of the values obtained for the second (S_{R_2}) and third order (S_{R_3}) terms using the full expression for λS_R as given by Eq. (B.20).

y	θ	S_{R_2}	S_{R_3}
mm			
.088	.268	1.15	5.67
.115	.318	2.4×10^{-1}	6.1×10^{-1}
.147	.368	6.3×10^{-2}	8.3×10^{-2}
.182	.418	1.7×10^{-2}	1.4×10^{-2}
.222	.467	5.6×10^{-3}	2.5×10^{-3}
.279	.516	1.9×10^{-3}	5.5×10^{-4}
.337	.650	1.2×10^{-4}	1.0×10^{-5}
.526	.793	6.1×10^{-6}	1.4×10^{-7}
.716	.889	4.8×10^{-7}	4.0×10^{-9}
.952	.947	4.5×10^{-8}	1.5×10^{-10}
1.32	.985	1.2×10^{-9}	1.2×10^{-12}

Table 4. Second and Third Order Contributions to Refractive Error Fringe Shift for Run 152.

In this example it appears that this method breaks down somewhere between .115 and .147 mm's from the wall because S_{R_3} becomes greater than S_{R_2}. However, as Fig. 12 shows, the last visible fringe for this particular run is at a value of $y_E = .251$ mm. At this point, as Table 4 shows, the refractive fringe shift error is much less than the uncertainty (0.025) in measuring the full fringe shift and hence can be neglected.

In order to estimate the extent of the "blind" region near the end wall, which was assumed to be due to light rays bending sufficiently to hit the wall, the value of y_E corresponding to the last light ray to miss the wall was computed from Eq. (B.5). Since

it has already been shown that this method, at least for the S_R series expansion, breaks down as $y \to 0$ this calculation of a ray trajectory for small y can at best be expected to give only a rough estimate of the extent of the "blind" region. The value of y_E was computed by starting at the wall ($y_E = 0$) and computing W_C from Eq. (B.5) for small steps in y_E. The first point at which $y_E \geq W_C$ corresponds to the location of the first entrance ray which misses the wall. Three terms were included in this calculation ($O(Z^6)$) and the a_i coefficients were expressed in terms of the b_i's by using Eqs. (B.9). This computation was made for each of the runs listed in Table 3 and in all cases the location of the first ray to miss the wall was between 0.11 and 0.15 mm. This order of magnitude for the region of confusion near the wall is consistent with the experimental observations.

As was discussed in Appendix B there are distortion effects caused by the refraction in the test section. It was shown there that the magnitude of the distortion depends on the distance from the wall surface. This dependence on entrance ray location appears in the b_i coefficients and Eq. (B.26) gives the distortion as

$$D_y = - b_1 D^2 \left\{ \left(\frac{1}{2} - \alpha\right) + \left(\frac{b_1^2 + 2b_2}{24} \right) (1 - 4\alpha) D^2 + \left(\frac{b_1^4 + 22 b_1^2 b_2 + 18 b_1 b_3 + 4 b_2^2}{720} \right) (1 - 6\alpha) D^4 + O(D^6) \right\} . \tag{6.25}$$

Here one should note that $\alpha = 1/3$ does not eliminate the first order contribution to distortion as it did for the refractive error fringe shift. However, the second and third order terms of Eq. (6.25) are

negative and tend to decrease the main first order contribution. Again the distortion increases close to the wall and falls off rapidly near the outer edge of the boundary layer. Table 5 lists the distortion computed for run 152 (data shown in Fig. 12) using the full expression given by Eq. (6.25) with $\alpha = 1/3$.

y mm	θ	Distortion mm
.044	.169	-2.55×10^{1}
.085	.264	-3.06×10^{-1}
.182	.418	-2.16×10^{-2}
.222	.467	-1.77×10^{-2}
.279	.516	-1.38×10^{-2}
.337	.650	-6.56×10^{-3}
.526	.793	-2.73×10^{-3}
.716	.889	-1.24×10^{-3}
.952	.947	-5.75×10^{-4}
1.32	.985	-1.69×10^{-4}

Table 5. Variation of Distortion with Distance from End Wall for Run 152.

The last visible data point for run 152 corresponds to $\theta = 0.52$ and Table 5 shows that the distorion for this point is less than 0.013 mm. Since this distortion is much less than uncertainty in locating the correct position for any fringe profile (±.03 mm) it is neglected in reducing the data. Because of the rather complicated way in which the b_i coefficients dependent on the parameters of each experiment the

distortion corresponding to the last data point is computed for each run listed in Table 3. Table 6 lists these results.

RUN #	y	θ	Distortion mm
164	.368	.765	-9.53×10^{-3}
162	.380	.839	-9.63×10^{-3}
163	.370	.757	-1.19×10^{-2}
161	.368	.764	-9.50×10^{-3}
160	.366	.714	-1.11×10^{-2}
159	.296	.732	-1.10×10^{-2}
156	.519	.766	-5.99×10^{-3}
155	.584	.710	-6.26×10^{-3}
154	.548	.651	-7.65×10^{-3}
153	.407	.688	-7.70×10^{-3}
149	.355	.561	-1.17×10^{-2}
150	.400	.587	-9.29×10^{-3}
146	.495	.696	-4.74×10^{-3}
145	.438	.633	-6.65×10^{-3}
144	.406	.609	-7.95×10^{-3}
157	.689	.751	-3.16×10^{-3}
143	.623	.664	-4.83×10^{-3}
166	.157	.682	-1.11×10^{-2}

Table 6. Distortion for All Runs Computed for the Last Visible Fringe Profile.

Here it is clear that the distortion for all runs is much smaller than the reading uncertainty and hence can be safely neglected.

Table 7 shows a similar listing of all of the different contributions to fringe shift error calculated for the last visible data point for each run given in Table 3. S_{R_2} and S_{R_3} in the table are the fringe shift error due to refraction as previously discussed. S_{BL} is the equivalent fringe shift error for the side wall boundary layers derived in Appendix C and S_{BS} is the fringe shift error due to the test beam passing through the last beam splitter of the MZI. This contribution is computed from the formulas given by Kahl and Mylin.[48] The last column in Table 7 is for the total refractive error fringe shift given by the sum of the four separate contributions. From this column it is clear that the combined effect of the three separate fringe shift errors is still much less than the reading error ($\pm.025$) and hence can be neglected. This conclusion is not true for run 166 which was recorded 21 μsec after reflection and this data is not included in the present compution of ν.

RUN #	y mm	θ	S_{R_2}	S_{R_3}	S_{BL}	S_{BS}	S_{TOTAL}
164	.368	.765	1.8×10^{-3}	4.5×10^{-4}	7.0×10^{-4}	2.9×10^{-4}	3.2×10^{-3}
162	.380	.839	5.8×10^{-4}	9.7×10^{-5}	6.1×10^{-4}	3.1×10^{-4}	1.6×10^{-3}
163	.370	.757	1.0×10^{-3}	2.2×10^{-4}	5.0×10^{-4}	2.0×10^{-4}	1.9×10^{-3}
161	.368	.764	4.9×10^{-4}	7.4×10^{-5}	6.9×10^{-4}	2.9×10^{-4}	1.6×10^{-3}
160	.366	.714	8.7×10^{-4}	2.7×10^{-5}	5.0×10^{-4}	4.2×10^{-4}	1.8×10^{-3}
159	.296	.732	1.0×10^{-3}	2.3×10^{-4}	6.1×10^{-4}	4.3×10^{-4}	2.3×10^{-3}
156	.519	.760	9.1×10^{-5}	6.5×10^{-6}	6.5×10^{-5}	6.0×10^{-5}	2.2×10^{-4}
155	.584	.710	9.5×10^{-5}	6.7×10^{-6}	6.5×10^{-5}	9.1×10^{-5}	2.6×10^{-4}
154	.548	.651	2.0×10^{-4}	2.0×10^{-5}	5.0×10^{-4}	1.8×10^{-4}	9.0×10^{-4}
153	.355	.561	1.0×10^{-3}	2.2×10^{-4}	4.5×10^{-4}	6.8×10^{-4}	2.3×10^{-3}
150	.400	.587	4.2×10^{-4}	6.1×10^{-5}	5.0×10^{-4}	2.8×10^{-4}	1.3×10^{-3}
146	.495	.696	4.3×10^{-5}	2.4×10^{-6}	8.8×10^{-5}	6.7×10^{-5}	2.0×10^{-4}
145	.438	.633	1.4×10^{-4}	1.4×10^{-5}	5.7×10^{-4}	1.3×10^{-4}	8.5×10^{-4}
144	.406	.609	2.8×10^{-4}	3.7×10^{-5}	6.0×10^{-5}	2.0×10^{-4}	5.8×10^{-4}
157	.689	.751	1.0×10^{-4}	3.5×10^{-7}	3.3×10^{-4}	2.9×10^{-5}	4.6×10^{-4}
143	.623	.664	4.6×10^{-5}	2.7×10^{-6}	5.1×10^{-5}	6.9×10^{-5}	1.7×10^{-4}
166	.157	.682	3.9×10^{-2}	4.6×10^{-2}	5.0×10^{-4}	3.9×10^{-2}	1.2×10^{-2}

Table 7. Summary of All Fringe Shift Errors

7. DISCUSSION AND CONCLUSIONS

The main result obtained in this study is the exponent ν of the assumed power law temperature dependence for thermal conductivity. Experimental temperature profiles, obtained interferometrically, were compared with a numerical solution of the full thermal boundary layer equation and a value of ν is established statistically from this comparison. As a prerequisite to the thermal boundary layer measurements the thermodynamic state of the gas behind the reflected shock was investigated in a series of time-resolved and snap-shot interferograms. From these experiments it was concluded that the state variables were adequately described with simple shock tube theory assuming frozen flow conditions.

As discussed in Section 3 the approximation of a power law temperature dependence for thermal conductivity over the temperature range 1000 to 10000°K is in good agreement with the theoretical predictions (taking $\nu = 3/4$), of Amdur and Mason.[28] This type of power law has been used to deduce values of ν from the end wall heat transfer experiments[9-11,49] and the reflected shock perturbation experiment of Sturtevant and Slachmuylders.[12]

At least squares fit for the data obtained in the present experiments indicates that the exponent in the power law temperature dependence for argon should be 0.668. That is,

$$\frac{K}{K_w} = \left(\frac{T}{T_w}\right)^{0.668 \pm .02}$$

where

$$K_w = 4.25 \times 10^{-5} \text{ cal. cm}^{-1} \text{ sec}^{-1} {}^{o}\text{K}^{-1}$$

and

$T_w = 300^{\circ}K$.

Figure 16 shows a comparison between values of thermal conductivity computed with the 3/4 power law and the experimental value given above. The values are shown on a logarithmic scale where the slope is ν. The two other curves on this figure are the smoothed experimental results of Collins and Menard[9] and the theoretical results using a Lennard-Jones 6-12 potential, after Hirschfelder, Curtiss, and Bird.[29] For the experiments in argon there is a considerable range in the final reported values of ν. Thus, Sturtevant and Slachmuylders[12] found good agreement between theory and experiment for $\nu = 0.81 \pm .02$, while Camac and Feinberg[11] reported $\nu = 0.76 \pm .03$ and Collins and Menard[9] give $\nu = 0.703$. In the later two cases the final value of ν is obtained as a mean of a large number of experiments where the individually determined values vary between 0.60 and 0.90. As Lauver[50] points out the reason for this large scatter is that an error of $0.2^{\circ}K$ in measuring the surface temperature rise (at 1 atm. pressure) or an error of $100^{\circ}K$ in T_5 at $5000^{\circ}K$ is equivalent to a 20% change in thermal conductivity. Figure 17 shows the scatter for the individual values of ν obtained from each of the present experiments. The scatter here is approximately ±7% and this represents a considerable improvement over the values reported from measurements of total heat flux at the end wall surface.

The value of ν obtained here is 5% lower than the lowest value reported for argon[19] from the end wall heat transfer measurements. However, at the lowest free stream temperature used here ($3150^{\circ}K$) good

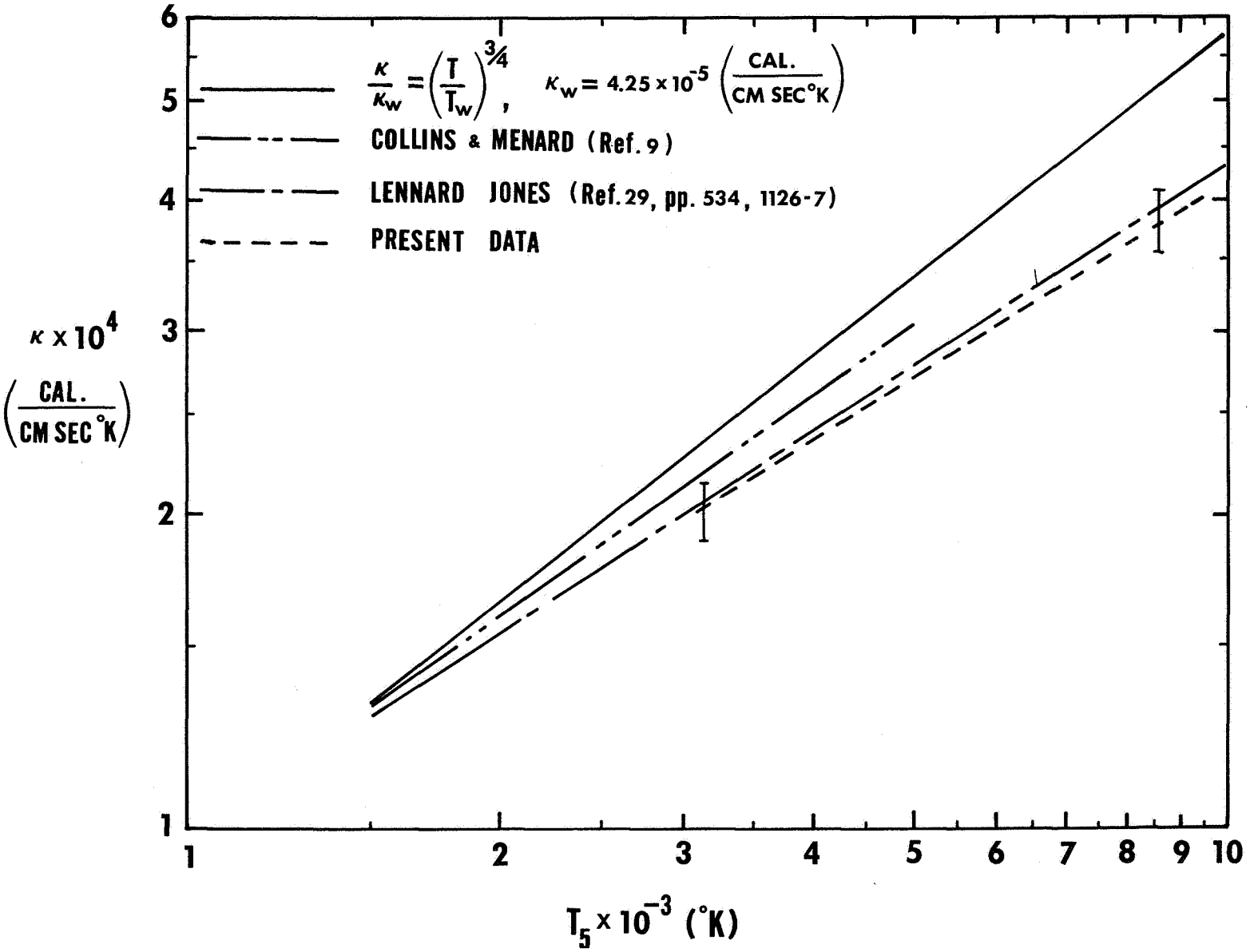

Fig. 16. Variation of Thermal Conductivity with Temperature

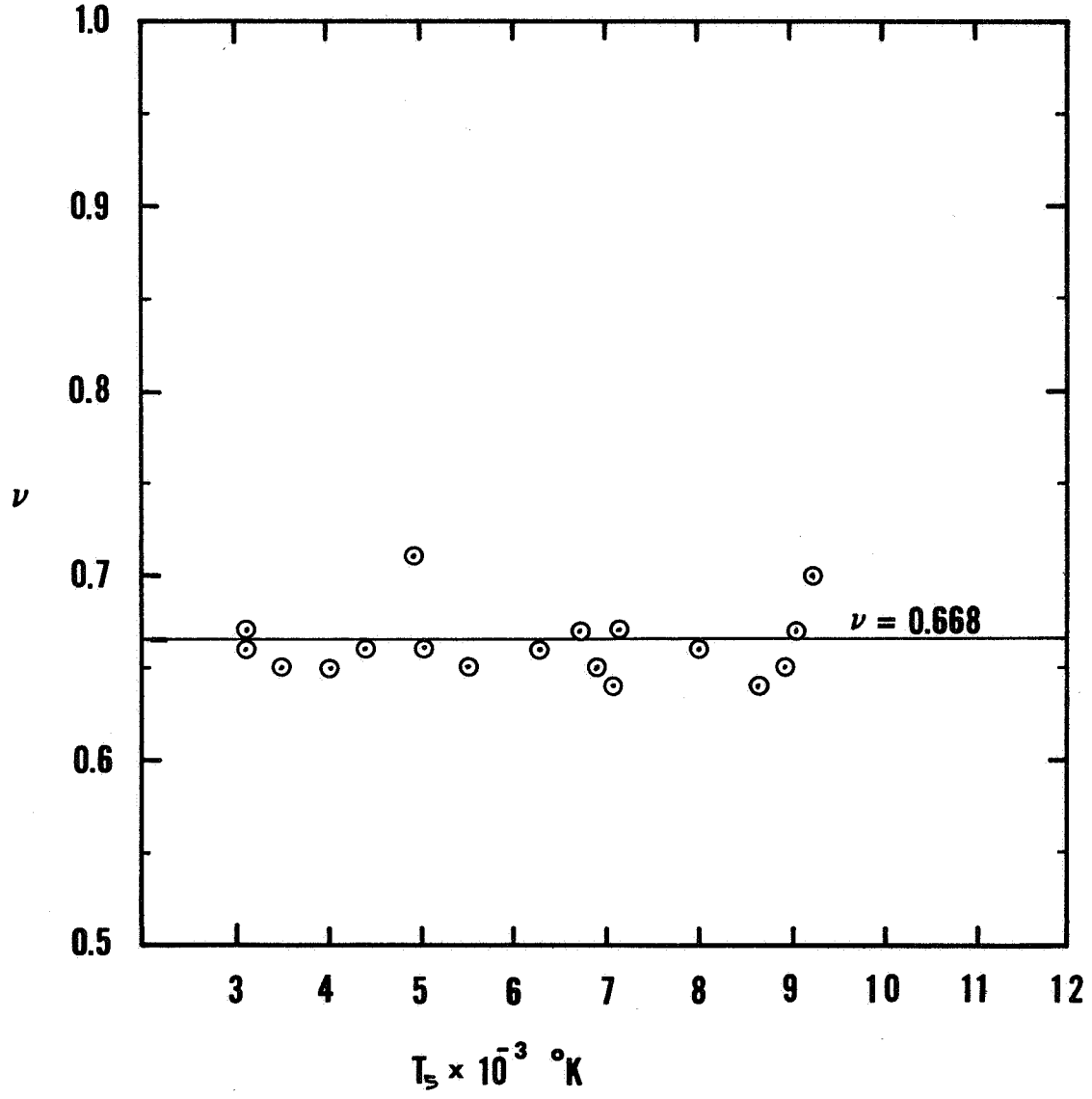

FIG. 17 EXPERIMENTAL VALUES OF ν OBTAINED FROM COMPARISON WITH THEORY

agreement exists between the present values for thermal conductivity and those reported by Smiley.[4] There are a number of possible sources of error in this experiment as indicated in the four appendices and one separate chapter devoted to a discussion of different types of interferometric error. In all cases the interferometric errors were larger approaching the end wall but they were still much smaller than the uncertainties in data reduction and hence would not explain the lower value of ν. It is felt that this lower value of ν in quantitative agreement with the Collins and Menard experiments gives additional confidence in concluding that the interaction potential assumed by Amdur and Mason does underestimate the short range potential. That is, the short range potential assumed in their work seems to weak. No conclusion can be drawn about the long range part of the potential because at the higher temperature this part of the potential has little influence on thermal conductivity.

In conclusion this method does reduce considerably the scatter in individual values of ν from one run to another, but, some further investigation will be required before it can be concluded that the average value of ν reported here is indeed in good agreement with the theory based on the best known interaction potentials. The method as outlined here and most of the techniques developed should be directly applicable to the case of ionized gases. It is straightforward to modify the snapshot techniques to simultaneously record at two-wavelengths. As has been demonstrated elsewhere[51,52] it is then possible to obtain simultaneous profiles of both electron density and mass density. In the present case, because of the constant pressure in the thermal layer, the two measurements can be combined to yield the profiles of degree of ionization and

temperature in the thermal layer. If the gas is in equilibrium in this layer then the present program could be used to analyze such profiles. Because of the contributions of the electrons and reactive components to the thermal conductivity it would not be possible to assume such a simple law for the variation of thermal conductivity with temperature. It would probably be preferable, in this case, to use a thermal conductivity theoretically computed as an initial approximation and to attempt to adjust the thermal conductivity to yield the correct profiles. Alternatively, one could use a function of temperature containing several parameters and vary these until good agreement with experiments is obtained. Of course, it would be necessary to use a function which is capable of reproducing the features of the theoretical thermal conductivity, in particular the maximum (vs. temperature) which occurs near 50% ionization.

REFERENCES

1. R. DiPippo, J. Kestin, and J. H. Whitelaw, Physica 32, 2064 (1966).
2. References to much of this work can be found in R. S. Devoto, Phys. Fluids 9, 1230 (1966).
3. R. S. Devoto, Phys. Fluids 10, 354 (1967).
4. E. F. Smiley, Ph.D. Thesis, Catholic University of America (1957).
5. C. F. Hansen, R. A. Early, F. E. Alzofon and F. C. Witteborn, NASA TR R-27 (1959).
6. T. C. Peng and W. F. Ahtye, NASA TN D-687 (1961).
7. T. A. Thompson, Australian Defense Scienfitic Service, Aerodynamics Note 186 (1960).
8. W. F. Ahtye and T. C. Peng, NASA TN D-1303 (1962).
9. D. J. Collins and W. A. Menard, J. of Heat Transfer 88, 52 (1966).
10. D. J. Collins, R. Greif and A. E. Bryson, Int. J. of Heat Mass Transfer 8, 1209 (1965).
11. M. Camac and R. M. Feinberg, J. Fluid Mech. 21, 673 (1965).
12. B. Sturtevant and E. Slachmuylers, Phys. Fluids 7, 1201 (1964).
13. G. Smeets, Z. für Naturforschung 20, 683 (1965).
14. M. Francon, Optical Interferometry (Academic Press, New York, 1966).
15. I. I. Glass and G. N. Patterson, J. Aero. Sci. 22, 73 (1955).
16. W. Bleakney, D. K. Weimer, and C. H. Fletcher, Rev. Sci. Instr. 20, 807 (1949).
17. I. I. Glass, W. A. Martin, and G. N. Patterson, UTIA Report No. 2, (1953).
18. H. Wong, Ph.D. Thesis, Stanford Univ., Stanford, Calif., (1964).

19. R. W. Ladenburg and D. Bershader, Physical Measurements in Gas Dynamics, (Princeton University Press, Princeton, 1954), Section A.3.

20. P. B. Gooderun, G. P. Wood and M. J. Brevourt, NACA TN 1857 (1949).

21. A. F. Klein, Physico-Chemical Diagnostics of Plasmas, AIAA, Fifth Biennial Gas Dynamics Symposium, (Northwestern University Press, Evanston, 1964), p. 233.

22. F. Bennett, D. Shear and J. Burden, J. Opt. Soc. Am. 50, 212 (1960).

23. K. P. Horn, Ph.D. Thesis, Stanford Univ., Stanford, California (1966).

24. P. E. Oettinger, Ph.D. Thesis, Stanford Univ., Stanford, California (1966).

25. L. H. Tanner, Aero. Div., N.P.L., Rept. No. 3069, p. 46 (1956).

26. F. A. Goldsworthy, J. Fluid Mech. 5, 164 (1959).

27. D. Baganoff, J. Fluid Mech. 23, 209 (1965).

28. I. Amdur and E. A. Mason, Phys. Fluids 1, 370 (1958).

29. J. O. Hirschfelder, C. F. Curtiss and R. B. Bird, Molecular Theory of Gases and Liquids, (John Wiley and Sons, Inc., New York, 1954).

30. L. Fox, Numerical Solution of Ordinary and Partial Differential Equations, (Pergamon Press, 1962) p. 24.

31. H. M. Kemp, Dept. Mech. Eng., Fluid Mech. Lab., M.I.T., Cambridge, Pub. No. 64-6 (1964).

32. R. E. Duff, Phys. Fluids 2, 207 (1959).

33. A. Roshko, Phys. Fluids 3, 835 (1960).

34. M. G. Dunn, Cornell Aeronautical Lab., Rept. No. AI-2187-8-3, Oct., (1966).

35. H. S. Friedman and J. A. Fay, Phys. Fluids 8, 1967 (1965).

36. H. Petschek and S. Byron, Ann. Phys. 1, 270 (1957).

37. G. Jaffe, Dispersion and Absorption, Handbook der Experimentalphysik, vol. XIX, p. 42.

38. G. P. Wachtell, Ph.D. Thesis, Princeton University (1951). (Abstract), Phys. Rev. 78, 333 (1950).

39. J. N. Bradley, Shock Waves in Chemistry and Physics, (John Wiley and Sons Inc., New York, 1962).

40. W. L. Howes and D. R. Buchele, NACA TN 3507 (1955).

41. R. E. Blue, NACA TN 2110 (1950).

42. D. B. Bershader, Rev. Sci. Instr. 20, 260 (1949).

43. F. J. Weyl, Naval Bureau of Ordnance, Washington, D. C. (1948).

44. L. A. DeFrate, Sc.D. Thesis, M.I.T. (1950).

45. W. L. Howes and D. R. Buchele, NACA TN 2693 (1952).

46. W. L. Howes and D. R. Buchele, NACA TN 3340 (1952).

47. W. L. Howes and D. R. Buchele, J. Opt. Soc. Am. 56, 1517 (1966).

48. G. D. Kahl and D. C. Mylin, J. Opt. Soc. Am., 55, 364 (1965).

49. J. A. Fay and N. H. Kemp, J. Fluid Mech. 21, 659 (1965).

50. M. R. Lauver, NASA TN D-2117 (1964).

51. H. Wong and D. Bershader, J. Fluid Mech. 26, 459 (1966).

52. K. P. Horn, H. Wong, and D. Bershader, J. Plasma Physics 1, 157 (1967).

53. F. J. Weinberg, Optics of Flames (Butterworth and Co. Ltd., London, 1963).

APPENDIX A

A-1. Alignment Procedure

The accuracy of interferometric measurements near an extended solid surface depends to a large extent on knowing that the collimated light of the interferometer test beam does indeed pass parallel to the surface. The method most often used for accomplishing this alignment is to observe the diffraction patterns produced on two sides of some object. Alignment is assured when the diffraction lines on each side of the object are equal in number, intensity, and spacing. A complete discussion of this technique is given in Refs. 44, 45, and 46.

An alternative method used in this study makes use of the spurious interference fringes which form adjacent to the solid surface when slight misalignment is present. The method was first proposed by Howes and Buchele[40] in their work on practical considerations of gas flow interferometry. The fringes which are observed in this technique can be characterized by the angle β illustrated in Fig. 18. For $\beta<0$ the spurious fringes are produced by a combination of the reflected beam and the edge diffraction at the camera edge of the surface. Likewise for $\beta>0$ they are due to edge diffraction at the light source edge of the solid surface. In all cases the spurious fringes are a result of interference between the reference beam of the interferometer and the edge diffraction ($\beta>0$) or the edge diffraction combined with the refracted beam ($\beta<0$).

Figure 19 shows four photographs which illustrate the observed spurious fringes. Figure 19a shows the end wall region for $\beta>>0$ when only the test beam is transmitted. The diffraction patterns, visible near the wall

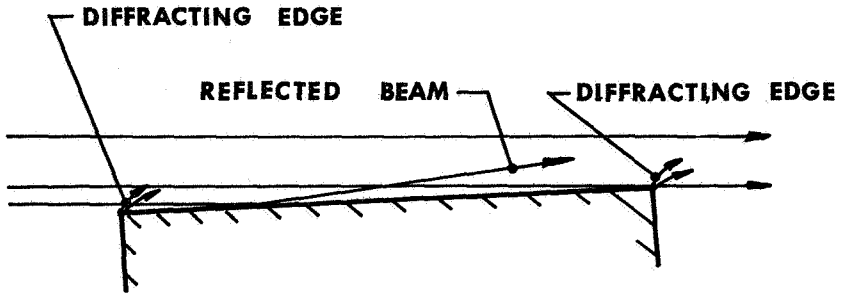

(a) $\beta < 0$

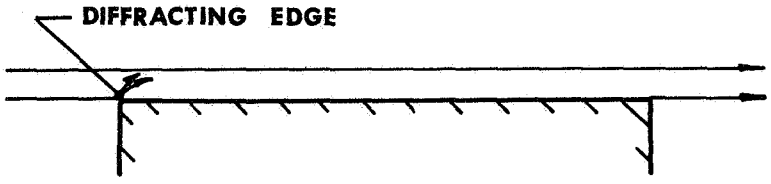

(b) $\beta = 0$

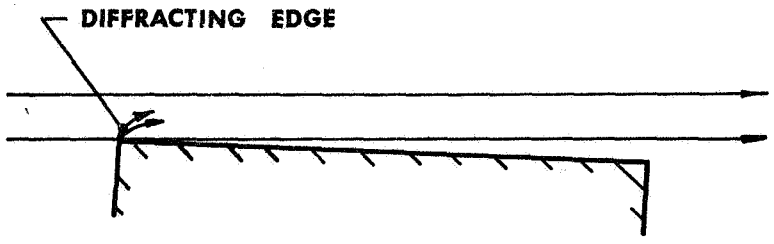

(c) $\beta > 0$

FIG.18 ILLUSTRATION OF END WALL ALIGNMENT PROCEDURE.

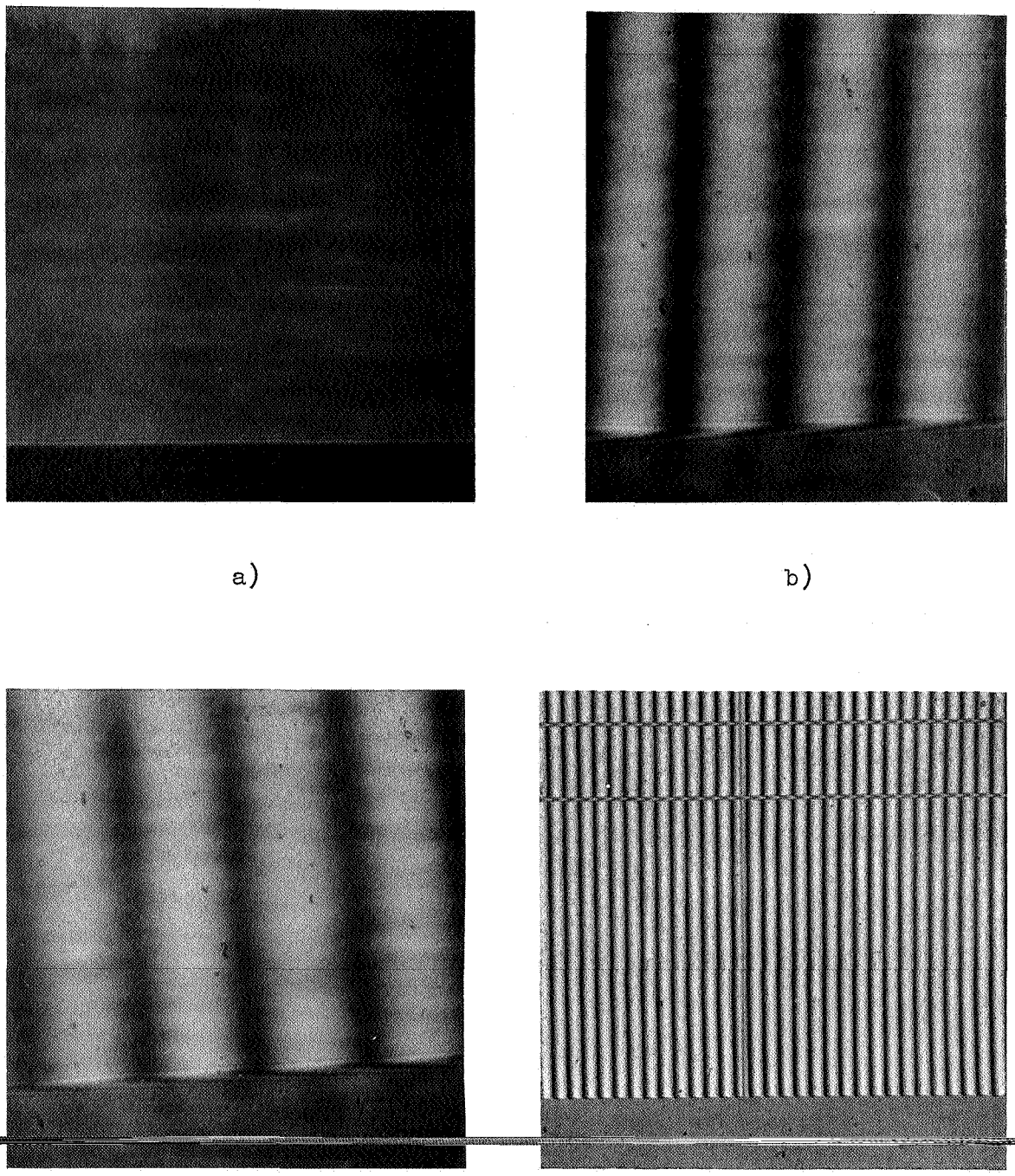

Fig. 19. Spurious Fringes Used in Alignment Procedure. a) Test Beam Transmitted for $\beta \gg 0$. b) Both Beams Transmitted for $\beta < 0$, Magnification ~ 30. c) Both Beams Transmitted for $\beta > 0$, Magnification ~ 30. d) Both Beams Transmitted for $\beta \sim 0$, Magnification ~ 2.3.

image, are formed by the light diffracted at the light source edge of the wall. The absence of any spurious fringes in this type of photograph gives assurance that they must be formed by interference with the reference beam.

Figure 19b shows the spurious fringes formed for $\beta<0$ when both beams of the interferometer are transmitted. This skewed pattern of fringes near the surface is probably caused by the light diffracted at the wall edge nearest the camera. This conclusion is based on two observations: First the skewed fringes are curved which would indicate that they are formed by light coming from several different angles and combining to form one curved fringe. Second, when $\beta<<0$ a completely different pattern of interference is observed. This new pattern shows a smeared series of very closely spaced fringes inclined at a very small angle with the wall. This type of interference is attributed to the reflected beam interfering with the compensating beam in a manner very much analogous to Lloyd's mirror fringes. When $\beta>>0$ there is no reflected beam and indeed this type of pattern does not occur.

Figure 19c shows the spurious fringes formed when $\beta>0$. In this case the same type of characteristic pattern which appears for $\beta<0$ is observed. The intensity of the skewed fringes is somewhat less in this case indicating the absence of the light contributed by the reflected beam.

When the light beam and the surface are aligned the skewed fringes disappear giving a pattern as shown in Fig. 19d. Notice here that at the root of each fringe a kind of periodic discontinuity is observed. Actually this same effect is visible before alignment is achieved. This effect was first attributed to the finite size of the light source and later this conclusion was confirmed by actually decreasing the light source aperture

until the discontinuities were no longer visible.

An estimate of the accuracy of this technique was obtained in the following manner. First the MZI was adjusted for $\beta \cong 0$ (no visible spurious fringes). Then the slide mechanism used to rotate the interferometer table was moved until the first visible spurious fringes appear. By knowing the linear travel of the slide mechanism and the pivot arm of the table support one finds that a misalignment of $\pm 2.5 \times 10^{-4}$ radians is clearly visible. Such a misalignment would result in a linear uncertainty of $\pm$ 0.01 mm for a given ray over the width of the test section. Thus a known misalignment results in a linear error of a given light ray which is smaller than the same type of error resulting from the use of a finite light source aperture.

APPENDIX B

B-1. Refractive Error Analysis

As described in Section 6, the method of Wachtell[38] has been used to compute the errors in the fringe shifts due to refraction of the light rays. This method will be reviewed and extended in this appendix. Furthen, a limited comparison will be made of the results of this method with the recently published analysis of Howes and Buchele[47]. Although these authors do not refer to Wachtell the two approaches are very similar but the method of presenting the results are quite different.

The fringes which are formed at the image plane (film plane) of the optical system can be thought of as the real image of virtual fringes located at an object plane within the test section of the shock tube. Assume now that the image plane of the optical system is focussed on the object plane P, shown in Figure 20, located at a distance h from the exit window. The object of this analysis is to find the value of h which minimizes the error in fringe shift caused by refraction and to compute the higher order corrections for the refractive errors.

A schematic diagram showing the paths of three different light rays, is shown in Fig. 20. When conditions in the test section are uniform, the light entering at E and F (all incident rays are assumed to be on the same wave front normal to the entrance window which is perpendicular to the end wall), will follow the straight paths FGH and ELM (shown dashed in Fig. 20). If however, there is a density gradient normal to the end wall the light ray entering at E will bend towards the wall and follow the curved trajectory ECD instead of the straight path ELM. If the fringes are focused on the plane P then the ray ECD will appear to

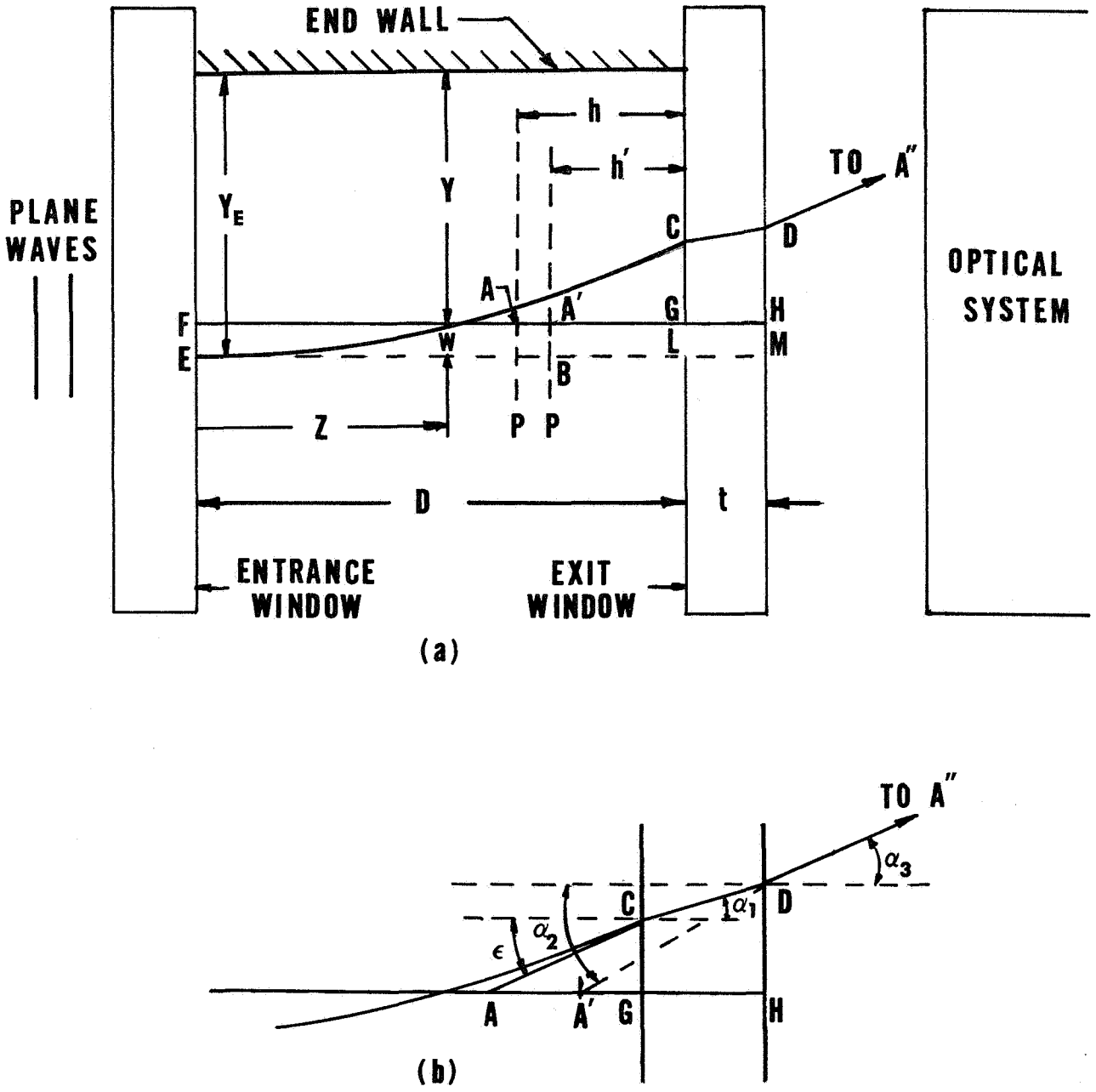

FIG. 20 ILLUSTRATION OF REFRATED (ECD) AND UNREFRACTED (ELM) LIGHT RAYS THROUGH THE THERMAL LAYER.

originate from point A. This point is found by constructing a tangent to the ray EC at C and extending this line until it intersects the plane P. The ray FGH is an undeviated ray passing through point A which will arrive at the same point (A") on the image plane as the refracted ray ECD. Thus, to a viewer at the image plane, ray ECDA" appears to follow the straight path FGHA". The error in fringe shift S_R caused by this effect is given by the optical path difference, in wavelengths, between these two rays measured from the light source to A".

Assuming the light enters perpendicular to the entrance window, there is no optical path difference for the two rays from the source up to the inside edge of the entrance window. Then the fringe shift error S_R is given by the difference in optical path between the actual ray ECDA" and the ray which would reach point A" on the screen if there were no refraction FGHA",

$$\lambda S_R = (ECDA")_{OPT} - (FGHA")_{OPT} \qquad (B.1)$$

$$=(EC)_{OPT} - (FG)_{OPT} + (CD)_{OPT} - (GH)_{OPT} + (DA")_{OPT} - (HA")_{OPT}$$

where the subscript OPT refers to the optical path. Here $(DA")_{OPT}$ and $(HA")_{OPT}$ depend on the particular optical system used but the difference $(DA")_{OPT} - (HA")_{OPT}$ is independent of the camera optics. This result can be demonstrated in the following way: Imagine the shock tube evacuated and replace the exit window with a material having a refractive index of unity. Plane P' will now be the object plane and h', the distance from the plane P' to the exit window, will be given by

$$h' + t = h + \frac{t}{n_g} \qquad (B.2)$$

where n_g is the refractive index of the exit window and t is the thickness of this window. Under these conditions A" will be the image of A' (located by a backward extension of the exit ray DA") and the rays leaving A' in any direction will arrive at A". That is, the optical distance from A' to A" will be independent of the direction in which rays leave A' and one can write

$$A'H + (HA")_{OPT} = A'D + (DA")_{OPT}$$

or

$$(DA")_{OPT} - (HA")_{OPT} = A'H - A'D \tag{B.3}$$

which when substituted into Eq. (B.1) gives

$$\lambda S_R = (EC)_{OPT} - (FG)_{OPT} + (CD)_{OPT} - (GH)_{OPT} + A'H - A'D \tag{B.4}$$

Note here that details of the camera optics no longer remain in the expression for S_R.

In order to compute the quantities in this expression the following assumptions are made:

(A). Density and hence n in the boundary layer depend only on the distance from the wall y.

(B). The deflection of a light ray from a straight line can be expressed as a power series in Z, the distance from the entrance window,

$$W = a_o + a_1 Z + a_2 Z^2 \tag{B.5}$$

As it turns out all the odd coefficients in this series

$(a_1, a_3, a_5,)$ as well as a_o are zero. Thus, the deviation W from a straight line is a parabola in the lowest approximation. In the present analysis the first three non-vanishing terms will be included (i.e., up to Z^6) in this series.

(C). n can be expressed as a power series in the deviation W from an unrefracted ray,

$$\frac{n}{n_E} = 1 + b_1 W + b_2 W^2 + \qquad \text{(B.6)}$$

Here the expression for n is normalized with the value of n at the entrance station n_E. Thus, the first term in the expression is unity because at the entrance station the ray is unrefracted and W is zero.

The path of a light ray through the boundary layer can be calculated from the law of refraction for a non-homogeneous medium which is given by[53]

$$\frac{dn}{n} = \frac{W''}{1 + (W')^2}\, dW \qquad \text{(B.7)}$$

where the prime denotes differentiation with respect to Z. The boundary conditions for this equation are taken as

$$n = n_e,\ W = W' = 0,\ \text{at } Z = 0$$

which state that the refractive index at the entrance station E is just n_E and the deviation of the ray at this point is zero. The condition $W' = 0$ is a result of assuming the entrance ray normal to the window. The solution for Eq. (B.7) subject to the above boundary conditions is

$$\frac{n}{n_E} = [1 + (W')^2]^{\frac{1}{2}} . \qquad \text{(B.8)}$$

The boundary conditions for W show that a_o must be zero and by combining Eqs. (B.5), (B.6), and (B.8) one can show that

$$a_2 = \frac{b_1}{2},$$

$$a_4 = \frac{b_1^3 + b_1 b_2}{24}, \tag{B.9}$$

$$a_6 = \frac{b_1^5 + 22b_1^3 b_2 + 18b_1^2 b_3 + 4b_1 b_2^2}{720},$$

and that a_1, a_3, a_5 are all zero.

Now each term in Eq. (B.4) can be expressed as a power series in the test section width D by making use of assumptions (A), (B), and (C). Each term will be considered separately starting with $(EC)_{OPT}$ which is defined as

$$(EC)_{OPT} = \int_{EC} n \, ds \tag{B.10}$$

where ds is given by

$$ds = [1 + (W')^2]^{\frac{1}{2}} \, dz.$$

With this expression for ds and Eq. (B.8) the integral in Eq. (B.10) can be integrated from 0 to D giving

$$(EC)_{OPT} = n_E \left[D + \frac{4a_2^2}{3} D^3 + \frac{16a_2 a_4}{5} D^5 + \frac{16a_4^2 + 24a_2 a_6}{7} D^7 + \ldots \right] \tag{B.11}$$

The next term to evaluate in Eq. (B.4) is $(FG)_{OPT}$ which is given by

$$(FG)_{OPT} = n_A D$$

where n_A is the value of n at the point A. With the aid of Fig. 20b one can write

$$\tan \epsilon = W_c' = \left[\frac{n_c}{n_E}^2 - 1\right]^{\frac{1}{2}} \tag{B.12}$$

which gives a relationship between the value of n at point C and the value of n at the entrance station of ray ECD. Equation (B.8) was used to write the last term in Eq. (B.12).

Again referring to Fig. 20b one can write

$$W_A = W_C + t \tan \alpha_1 - (h' + t)\tan \alpha_2 \tag{B.13}$$

which, with the aid of Snell's law, can be expressed as

$$W_A = W_C + \frac{t \frac{n_E}{n_g} W_c'}{\left[1 - \frac{n_E^2}{n_g^2}(W_c')^2\right]^{\frac{1}{2}}} - \frac{(h' + t)\, n_E W_c'}{\left[1 - n_E^2 (W_c')^2\right]^{\frac{1}{2}}} \tag{B.14}$$

where $(h' + t)$ is given by Eq. (B.2), W_A is the deviation to point A, and W_c is the deviation at point C.

Substituting the expression for W_A into Eq. (B.6) gives n_A as a power series in D when one notes that W_C and W_C' can be expressed in terms of D through Eq. (B.5). Doing this and collecting terms the following power series for $(FG)_{OPT}$ is obtained

$$\frac{(FG)_{OPT}}{n_E} = D - (2b_1 h n_E a_2)D^2 + (b_1 a_2 + 4b_2 h^2 n_E^2 a_2^2)\, D^3$$

$$+ \left\{ \frac{4b_1 t n_E^3 a_2^3}{n_g} \left(\frac{1}{n_g^2} - 1 \right) - 4b_1 h n_E^3 a_2^3 - 4b_1 h n_E a_4 \right.$$

$$\left. - 4a^2 h n_E b_2 - 8b_3 h^3 n_E^3 a_2^3 \right\} D^4 + \left\{ b_1 a_4 + b_2 a_2^2 \right.$$

$$+ 16\, b_4 h^4 n_E^4 a_2^4 + 12\, b_3 h^2 n_E^2 a_2^3 - 4\, b_2 h\, n_E a_2 \left[\right.$$

$$\left. \left. \frac{4t n_E^3 a_2^3}{n_g} \left(\frac{1}{n_g^2} - 1 \right) - h\, n_E^3 a_2^3 - 4\, h\, n_E\, a_4 \right] \right\} D^5$$

$$+ O\,(D^6). \qquad \text{(B.15)}$$

Next consider the term $(CD)_{OPT} - (GH)_{OPT}$ which, with the aid of Fig. 20b, can be written as

$$(CD)_{OPT} - (GH)_{OPT} = n_g t \left(\frac{1}{\cos \alpha_1} - 1 \right). \qquad \text{(B.16)}$$

A power series expansion for Eq. (B.16) is obtained with the aid of Snell's law, Fig. 20b, and Eq. (B.12), where $\cos \alpha_2$ can be written as

$$\cos \alpha_2 = \left[1 - \left(\frac{n_E}{n_g} \right)^2 (W_c')^2 \right]^{\frac{1}{2}} \qquad \text{(B.17)}$$

from which one can write

$$\frac{1}{\cos \alpha_1} = 1 + \frac{1}{2} \frac{n_E^2}{n_g^2} (W_c')^2 + \frac{3}{8} \frac{n_E^4}{n_g^4} (W_c')^4$$

$$+ O \left[(W_c')^6 \right].$$

Again using Eq. (B.5) to write W_c' as a power series in D one can write Eq. (B.16) as

$$(CD)_{OPT} - (GG)_{OPT} = \frac{2\, n_E^2\, t\, a_2^2}{n_g}\, D^2 + \left[\frac{8\, a_2 a_4 t n_E^2}{n_g} + \frac{6\, n_E^4\, t\, a_2^4}{n_g^3} \right] D^4 + 0\,(D^6). \tag{B.18}$$

The final two terms of Eq. (B.4) are written in a power series in D in a manner similar to that used to write Eq. (B.18). That is, using Fig. 20b one writes

$$A'H - A'D = (h' + t) \left[1 - \frac{1}{\cos \alpha_2} \right]$$

which can also be expressed as

$$A'H - A'D = -\left(2\, h\, n_E^2\, a_2^2 + \frac{2t\, n_E^2 a_2^2}{n_g} \right) D^2$$

$$- \left(6\, h\, n_E^4 a_2^4 + 8h\, n_E^2\, a_2 a_4 + \frac{6t}{n_g}\, n_E^4 a_2^4 \right.$$

$$\left. + \frac{8t}{n_g}\, n_E^2\, a_2 a_4 \right) D^4 + 0\,(D^6) \tag{B.19}$$

This now concludes the evaluation of the terms in Eq. (B.4). Each of the optical paths have been written as power series in D with certain other quantities which are defined either in Fig. 20 or in assumptions (A) through (C). Substituting the expressions from Eqs. (B.11), (B.15), (B.18), and (B.19) into (B.4) gives the following form for λS_R

$$\lambda S_R = \left(\frac{\alpha\, b_1^2}{2} - \frac{b_1^2}{6}\right) D^3 + \left[- b_1^2\, b_2 \alpha^2 + \frac{b_1^4\, \alpha}{8} + b_1^2\, b_2 \alpha \right.$$

$$\left. + \frac{b_1^4}{40} - \frac{b_1^2 b_2}{5} - \frac{b_1^4\, \beta}{8}\left(\frac{1}{n_g^2} - 1\right)\right] D^5 +$$

$$\left[\left(\alpha^3 - \frac{3\alpha^2}{2} + \frac{3\alpha}{4} - \frac{3}{28}\right) b_1^3 b_3 + \left(-\frac{4\alpha^2}{3} + \frac{25\alpha}{36} - \frac{1}{252}\right) b_1^4\, b_2 \right.$$

$$+ \left(-\frac{2}{3}\alpha^2 + \frac{4\alpha}{9} - \frac{4}{63}\right) b_1^2 b_2^2 + \left(\frac{1}{2} - \alpha + \frac{2\alpha - 1}{2n_g^2}\right) b_1^4 b_2 \beta$$

$$\left. + \left(\frac{7\alpha}{144} + \frac{\beta}{16} - \frac{\beta}{16 n_g^4} + \frac{5}{1008}\right) b_1^6 \right] D^7 + O(D^9) \qquad \text{(B.20)}$$

where α and β are defined by

$$\alpha = \frac{h}{D}, \qquad \beta = \frac{t}{n_g D}$$

and the a_i's have been written in terms of b_1, b_2, and b_3 from Eq. (B.9). In all of the expressions used in writing Eq. (B.20) n_E appears as a multiplicative factor and since n is always very near unity (differing by a term of order 10^{-3}) n_E has been set equal to 1. This expression is identical with that given by Wachtell[38] as Eq. (IIA-17) if $n_E = 1$. Howes and Buchele[47] have also derived an expression similar to Eq. (B.20) for evaluating refractive errors. Their results are given by an integral expression involving the various angles which the refracted ray makes with respect to the coordinate axis. Unfortunately there doesn't seem to be an easy way to reduce their result to a form convenient for comparison with Eq. (B.20). However, it is possible to compare their results with this work in two limiting cases. These limiting cases are characterized by

the number of terms utilized in the series given by Eq. (B.6) and this comparison will be made after a brief discussion of the distortion in Section B.2.

The b_1, b_2 and b_3 coefficients in Eq. (B.20) can be expressed as derivatives of density from Eq. (B.6). That is,

$$b_1 = \frac{1}{n_E}\frac{dn}{dW}\Big|_{W=o} = K\frac{d\rho}{dY}\Big|_{Y=Y_E}, \tag{B.21}$$

$$b_2 = \frac{1}{2n_E}\frac{d^2n}{dW^2}\Big|_{W=0} = \frac{K}{2}\frac{d^2\rho}{dY^2}\Big|_{Y=Y_E}, \tag{B.22}$$

and

$$b_3 = \frac{1}{6n_E}\frac{d^3n}{dW^3}\Big|_{W=0} = \frac{K}{6}\frac{d^3\rho}{dY^3}\Big|_{Y=Y_E} \tag{B.23}$$

where the second expression is written by using Eq. (5.2) and n_E is taken as unity. Given in this form it is clear that the b_i's depend on the particular light ray under consideration since $W = o$ when $Y = Y_E$.

B.2 Distortion

When viewed by an observer from the region $Z > D$ the refracted light ray ECD appears to originate at the apparent object point A' shown in Fig. 20. If the refractive index were constant ray ECD would follow ray ELM and A" would be the image of point B. The separation between these two apparent object points D_Y, see Fig. 21, represents a distortion of the apparent object point associated with ray ECD. This distortion is due to refraction and a method for evaluating its magnitude follows.

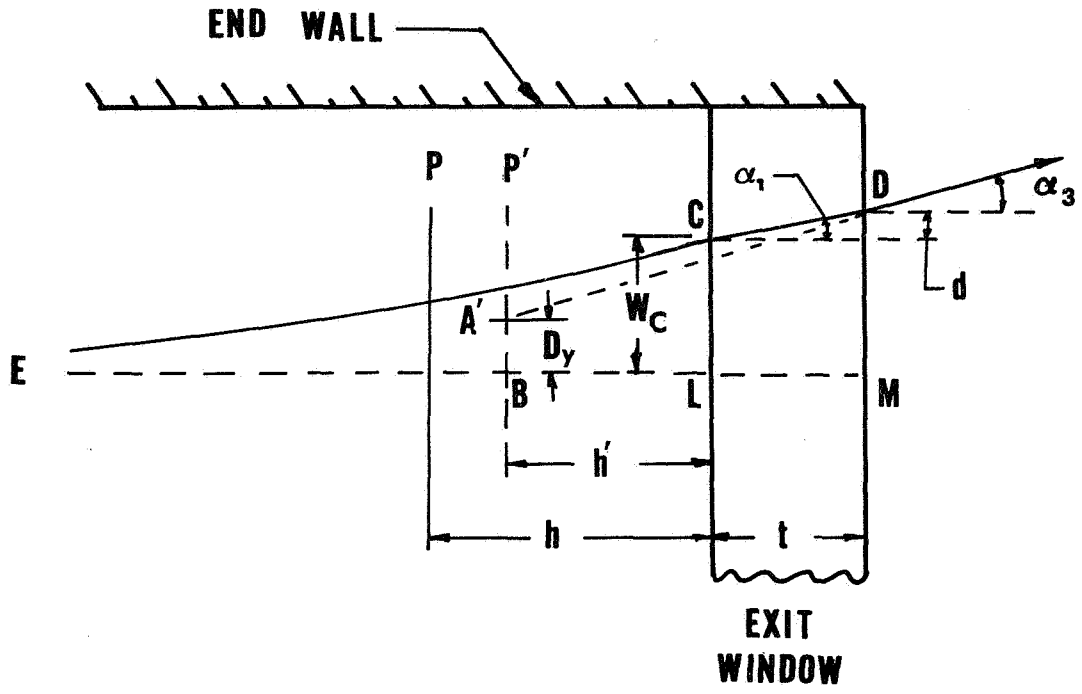

FIG. 21 ILLUSTRATION OF DISTORTION CAUSED BY REFRACTION.

By inspection of Fig. 21 D_y can be written as

$$D_y = W_c + d - (h' + t) \tan \alpha_3 \qquad (B.24)$$

where W_c can be expressed as a power series in D by using Eq. (B.5) and noting that Z = D at the exit window. Assuming small angles of incidence for the refracted rays, using Eq. (B.2) to express (h' + t), and noting that α_3 is equal to ϵ Eq. (B.24) can be rewritten as

$$D_y = W_D - h \tan \epsilon. \qquad (B.25)$$

When this is expressed in a power series in D (refer to method used in writing Eq. (B.18)) one finds

$$D_y = \left(\frac{b_1}{2} - b_1\alpha\right) D^2 + \left(\frac{b_1^3 + 2b_1b_2}{24}\right)\left(1 - 4\alpha\right) D^4 + \left(\frac{b_1^5 + 22b_1^3b_2 + 18b_1^2 b_3 + 4b_1b_2^2}{720}\right)\left(1 - 6\alpha\right) D^6 + O(D^8). \qquad (B.26)$$

With this expression for distortion and Eq. (B.20) for the refractive error correction due to the increased path length the comparison, mentioned in the previous section, with the Howes and Buchele[47] results can now be made.

First consider a one term approximation which corresponds to $n/n_E = 1$ or a constant refractive index along each ray. Under this condition the rays are straight lines and all the b_i's are zero. From Eq.'s (B.26) and (B.20) D_y and S_R must be zero. This is in agreement with the one-term approximation given by Eq.'s (52) and (53) of Ref. 47. The second comparison can be made with the two term approximation $n/n_E = 1 + b_1W$

which corresponds to a linear variation of refractive index and keeping the same order of terms, a parabolic trajectory for each light ray within the test section. For this case

$$\lambda S_R = \left(\frac{\alpha}{2} - \frac{1}{6}\right) b_1^2 D^3 \tag{B.27}$$

and

$$D_y = \left(\frac{b_1}{2} - b_1\alpha\right) D^2 \tag{B.28}$$

where these terms are given by the leading terms in the power series expansion. From Eq. (B.27) we see that when $\alpha = 1/3$ the refractive error contribution is zero. However, Eq. (B.28) shows that distortion is zero for $\alpha = 1/2$. These conclusions are consistant with Eqs. (54) and (55) of Ref. 47.

For the present experiments α was chosen as 1/3 in order to minimize the refractive errors due to the light rays bending and traveling over a a longer path length. However, for each case the higher order contributions to both S_R and D_y have been computed and the results are presented in Section 6.

APPENDIX C

C-1. Window Boundary Layer Analysis

In Section 4.1 it has been shown that the fringe shift at a point in the boundary layer, defined by coordinates (x,y) is related to conditions in the assumed uniform region 5 by

$$\lambda S(x,y) = \int_0^{\ell} \left[\eta(x,y,z) - \eta(x_5,y_5,z_5)\right] dz. \qquad (C.1)$$

If one then assumes that n is independent of z the following expression for density at the point (x,y) is given by Eq. (4.4)

$$\rho(x,y) = \frac{\lambda}{K\ell} S(x,y) + \rho_5. \qquad (C.2)$$

This assumption is not strictly true because, in fact, there are side wall boundary layers on each of the viewing windows. The objective of this analysis is to give a method for estimating the total contribution of these boundary layers to the measured density distribution and then to express this in terms of an equivalent fringe shift (S_{BL}) which can then be compared to the other fringe shifts errors.

As was shown in Appendix B the gradients of refractive index in the boundary layer can cause refraction of the light rays which must be considered when using Eq. (C.2) to compute $\rho(x,y)$. It was also concluded in Section 6 that, for the present case, these errors were much less than the uncertainty in measuring fringe shifts and hence could be neglected. However, in order to keep this treatment general the possibility of refractive errors will be considered.

The contribution of window boundary layers can be determined by imagining a hypothetical situation in which refractive errors do contribute to the measured fringe shift but no boundary layers are present.

For this situation ρ_{IND} represent the computed density which would be given by Eq. (C.2) if an additional term is included which accounts for the refraction contribution. That is,

$$\rho_{IND} = \rho_5 + \frac{\lambda}{K\ell} S + \frac{\lambda}{K\ell} S_R \tag{C.3}$$

where $\frac{\lambda}{K\ell} S_R$ represents the contribution to the indicated density which results from refraction. Next consider the situation where boundary layers are present and for this case let $\overline{\rho_{IND}}$ represent the density obtained from an interferogram for this situation. In this case if we assume that the refractive errors are identical to those for the hypothetical case and denote the fringe shift by $\overline{S}$ then

$$\overline{\rho_{IND}} = \rho_5 + \frac{\lambda}{K\ell} \overline{S} + \frac{\lambda}{K\ell} S_R. \tag{C.4}$$

Now ρ_{IND} and $\overline{\rho_{IND}}$ will be different and this difference represents the side wall boundary layer contribution. In order to write an expression for this difference consider two rays of light, one traversing the free stream at the outer edge of the thermal layer and the other passing through the boundary layer. In this way the average density traversed by each beam can be expressed as

$$\rho_B = \frac{\rho_{AV}(\ell - 2\delta) + 2\int_0^{\delta} \rho(z)dz}{\ell} + \frac{\lambda}{K\ell} S_R \tag{C.5}$$

for the boundary layer and

$$\rho_F = \frac{\rho_5 (\ell - 2\delta_T) + 2\int_0^{\delta_T} \rho(z)\, dz}{\ell} \tag{C.6}$$

for the free stream. In Eqs. (C.5) and (C.6) δ_T represents the total thickness of the side wall boundary layer, δ the thickness of the side wall boundary layer in the region where it interacts with the end-wall

layer, and ρ_{AV} is the average value of density across the test section at the particular station in question. With this an expression for $\overline{\rho_{IND}}$ can be written by noting that the fringe shift $(\bar{S} + S_R)$ in Eq. (C.4), corresponds to a difference in density given by $(\rho_B - \rho_F)$. Using Eqs. (C.5) and (C.6) and changing the limits of integration in order to express the result in terms of a single integral one obtains:

$$\overline{\rho_{IND}} = \left(\rho_{AV} + \frac{\lambda}{K\ell} S_R\right) + \frac{2}{\ell}\left(\rho_5 \delta_T - \rho_{AV}\,\delta\right) - \frac{2}{\ell}\int_{\delta}^{\delta_T} \rho(z)dz \qquad (C.7)$$

With this expression the contribution of the window boundary layers $(\overline{\rho_{IND}} - \rho_{IND})$ can be expressed as

$$\frac{\overline{\rho_{IND}} - \rho_{IND}}{\rho_5} = \frac{\rho_{AV} - \rho_5 - \frac{\lambda}{K\ell} S}{\rho_5} + \frac{2\delta}{\ell}\left(\delta T - \frac{\rho_{AV}}{\rho_5}\right) - \frac{2}{\ell}\int_{\delta}^{\delta_T} \frac{\rho(z)}{\rho_5}\,dz \qquad (C.8)$$

Here one notes that the first term of this equation is always very small as long as refractive errors are small (see Eq. (C.3)) and in the limit $(S_R \to 0)$ ρ_{AV} will be identically ρ_{IND} and the term vanishes. For the present case where refractive errors are negligible a good first approximation for the window boundary layer will be given by

$$\frac{\overline{\rho_{IND}} - \rho_{IND}}{\rho_5} = \frac{2\delta}{\ell}\left(\frac{\delta_T}{\delta} - \frac{\rho_{AV}}{\rho_5}\right) - \frac{2}{\ell}\int_{\delta}^{\delta_T} \frac{\rho(z)}{\rho_5}\,dz \qquad (C.9)$$

In order to evaluate this expression one must make some assumption about the thickness of the side wall boundary layer. A first approximation would be to assume that the side wall boundary layer is identical to the end wall thermal layer. This is a conservative assumption because the

actual side wall boundary layer thickness behind the incident shock, over the region of observation, is much less than the thermal layer thickness.[39] The integral term in Eq. (C.9) is also conservatively evaluated by assuming a linear variation of ρ with distance (z) and a linear decrease of ρ_5 in the region where the side wall layer interacts with the end wall layer. Figure 22 shows a sketch illustrating this situation where δ_T has a constant value outside the thermal layer.

Strictly speaking Eq. (C.9) is valid only in the case where refractive errors are small and hence is not valid in the limit $\delta \to 0$. However, in the limit $\delta \to \delta_T$ where refractive errors are indeed small, since the gradient of refractive index is small, one can show that $\overline{\rho_{IND}}$ is just equal to ρ_{IND}. Thus the contributions to indicated density increase as one goes deeper into the end wall layer.

In order to be able to compare the window boundary layer contribution to the refractive error contribution one can define a fringe shift error S_{BL} which represents the influence of the side wall boundary layers. Using Eq. (C.9) S_{BL} is given by

$$\frac{\lambda}{\rho_5 K \delta} S_{BL} = \frac{\overline{\rho_{IND}} - \rho_{IND}}{\rho_5}$$

or

$$S_{BL} = \frac{2K}{\lambda} \rho_{AV} \delta_T \frac{\delta}{\ell} \left(\frac{\rho_5}{\rho_{AV}} - \frac{\delta}{\delta_T} \right) - \frac{2K}{\lambda} \frac{\delta}{\ell} \int_{\delta}^{\delta_T} \rho(z)\, dz. \qquad (C.10)$$

Values for S_{BL} are given in Section 6.

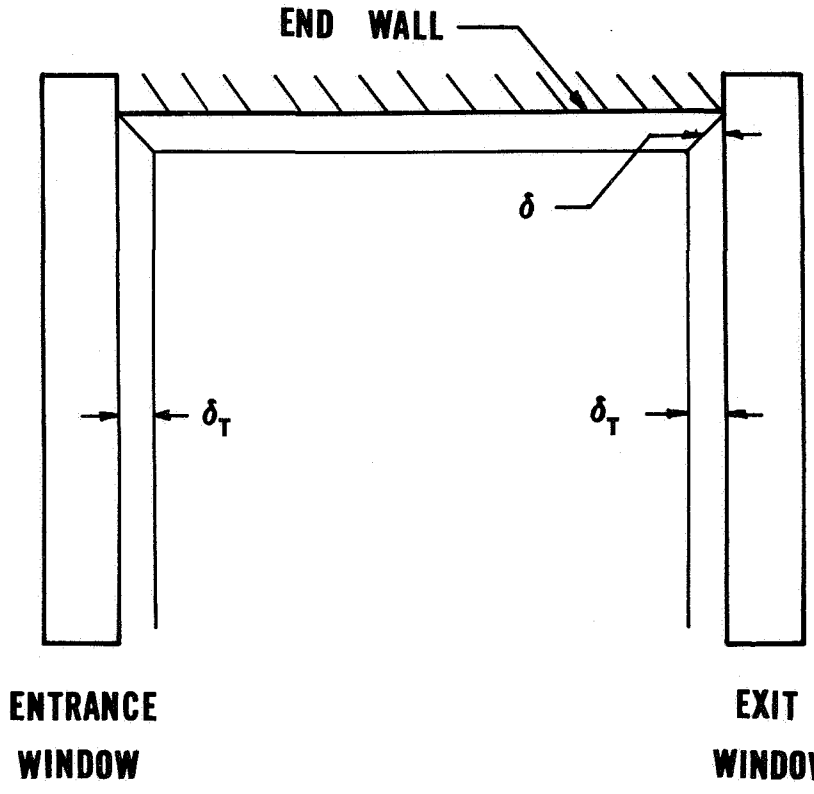

FIG. 22 ILLUSTRATION OF SIDE WALL BOUNDARY LAYER.